Three-dimensional shock wave reconstruction using multiple high-speed digital cameras and background oriented schlieren imaging

by

KYLE OAKLEY WINTER

Submitted in Partial Fulfillment
of the Requirements for the Degree of
Master of Science in Mechanical Engineering
with Specialization in Explosives Engineering

New Mexico Institute of Mining and Technology
Socorro, New Mexico
June, 2018

ABSTRACT

Arena tests are the standard method for quantifying explosive warhead performance. These tests typically measure a variety of performance characteristics, including shock wave speed and pressure, at a small number of locations. Interpolating between locations requires assuming a symmetric shock wave but frequently the results are difficult to interpret due to actual shock wave asymmetries or reflections within the arena environment. A methodology to perform three-dimensional reconstruction of an explosively-driven shock wave's position and shape as a function of time is developed here. A series of explosive tests are performed where the explosive process is imaged by multiple high-speed digital cameras spread over a wide area. The location and rotation of each camera is determined using a stereoscopic camera calibration procedure. The high speed images are processed using the background-oriented schlieren (BOS) method to visualize the shock wave. An automated shock wave detection algorithm was developed to determine the location of the shock in each BOS image. The two-dimensional shock wave pixel locations are scaled and rotated into three-dimensional locations using the information determined from the camera calibrations. The data from the multiple camera views are merged into a single three-dimensional point cloud representing the locations on the shock wave. For spherical shock waves a surface is fit to the point cloud which describes the location of the shock wave. Analysis of the shock wave surface allows shock wave asymmetries to be measured and tracked. The propagation of the shock wave is measured and used to predict the time of arrival and overpressure at different locations which are compared to measurements recorded by pressure gauges. The optical measurements agree with the pressure gauge measurements. The optical data was also able to identify the sources of peaks in the pressure data following the primary shock. The techniques developed here are shown to be useful tools that can be implemented to augment the traditional point-wise instrumentation of current explosives research testing and provide an enhanced characterization of an explosion over traditional arena test methods.

Keywords: Background-Oriented Schlieren (BOS); Shock Wave Detection; Three Dimensional Flow Reconstruction

ACKNOWLEDGMENTS

I would like to thank my incredible wife for supporting me in graduate school and all things.

I would also like to thank my adviser Dr. Michael Hargather for providing me the space and encouragement needed to grow and learn.

This work was funded by US Air Force SBIR Phase I contract F151- 174-1751 to Spectral Energies, LLC, with subcontractor Dr. Michael Hargather at New Mexico Institute of Mining and Technology.

CONTENTS

LIST OF TABLES

2

LIST OF FIGURES

NOMENCLATURE

ϵ	Schlieren system sensitivity or smallest angle of refraction that can be detected
γ	Ratio of the specific heats for the gas in which the shock is propagating
κ	Elementary rotation around Z axis
ω	Elementary rotation around X axis
τ	The distance from the refractive object to the camera
φ	Elementary rotation around Y axis
A	Dewey scaling parameter that represents the initial charge radius
a_0	Speed of sound at normal temperature and pressure
B	Dewey scaling parameter. Normally set to 1
C	Dewey scaling parameter
c	Sachs' time scale factor
$cold(x, y)$	The value of a pixel at location x,y in the reference image
D	Dewey scaling parameter
d	The apparent feature shift
$hot(x, y)$	The value of a pixel at location x,y in the analyzed image
L	The distance from the background to camera
M	Mach number
m_{ab}	The rotation matrix value at location (a, b)
P_1	Absolute pressure ahead of shock, which is assumed to be P_{atm}
P_2	Absolute pressure after the shock
P_{atm}	Atmospheric pressure

P_{over}	Overpressure or the absolute pressure after the shock wave minus the atmospheric pressure
$pic(x, y)$	The value recorded for location x,y in the new image
R	Measured shock radius
R_s	Scaled shock radius
S	Sachs' scale factor
T	Atmospheric temperature in K
t	Measured time
t_s	Scaled time
W	Mass of explosive
W_0	Reference explosive mass
BNC	Bayonet Neill-Concelman
BOS	Background oriented schlieren
IRIG	Inter-Range Instrumentation Group
PIV	Particle image velocimetry
TTL	Transistor-transitor logic

This thesis is accepted on behalf of the faculty of the Institute by the following committee:

Michael J. Hargather
Advisor

Jamie Kimberley

Chi Mai

I release this document to the New Mexico Institute of Mining and Technology.

KYLE OAKLEY WINTER Date

CHAPTER 1

INTRODUCTION

1.1 Research Motivation

The proliferation of high speed cameras and increases in computational power have improved how data are collected and analyzed from explosive testing. Traditionally, explosive performance data were collected as one dimensional functions of radius and the blast effects were assumed to be symmetric. This assumption holds in simple cases but is not valid for many complex modern systems. The recent development of large scale high speed refractive imaging allows for full field imaging of explosive events. Advancements in computational power and open source code allow for high speed and high fidelity data analysis. An automated methodology for extracting three-dimensional shock wave propagation information from multiple high-speed cameras is developed here.

1.2 Refractive Imaging Techniques

1.2.1 Schlieren

Schlieren systems are used to image differences in the refractive index of a material located within a test section. Schlieren and shadowgraph were first described in the 17th century by Robert Hooke. Schlieren was then rediscovered in the nineteen hundreds by August Toepler and has since been used widely for high-speed wind tunnel testing and laboratory investigations of explosives [1].

A traditional lens-type schlieren imaging system, which is shown in Figure 1.1, uses a simple parabolic lens to collimate light from a point source. The parallel light then passes through the test section and enters a second lens, which focuses the light to a point. A knife edge is placed at the focal point and a camera is placed behind the knife edge. When a refractive object enters the test section it bends the collomated light causing more or less interaction with the knife edge. The camera records the refractive index gradient as a gradient of bright to dark areas in the image. A schlieren image of the product gases from a lighter is shown in Figure 1.2. The figure demonstrates the sensitivity and resolution with which a schlieren system can capture a refractive object. This system is also capable of quantitatively measuring the refractive-index distributions within the test section [2]. These capabilities have made schlieren imaging a common laboratory tool. Schlieren is commonly used in super sonic wind tunnels and shock tubes to study compressible flow and is occasionally used in explosive field testing. The diameter of the test section is limited to the diameter of optics used. Lens schlieren systems are generally limited to 15 cm diameter due to cost of the lenses[3].

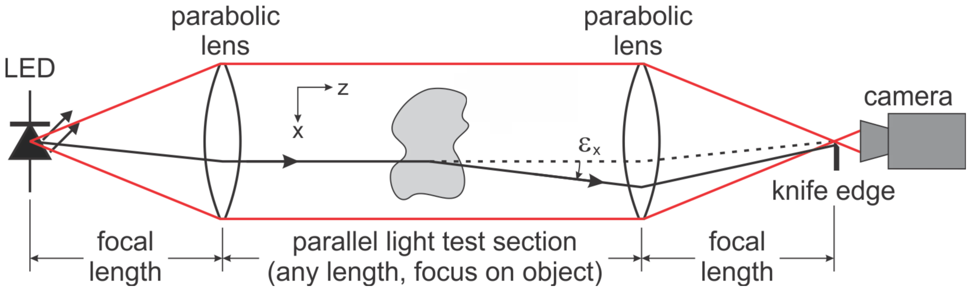

Figure 1.1: Diagram of typical lens schlieren system with light ray paths shown.

1.2.2 Shadowgraph

Shadowgraph systems are capable of imaging much larger areas than schlieren because no collimating optics are required, but lack the sensitivity and ability for quantitative density measurements that are possible with schlieren [3]. The difference between the two visualizations approaches can be seen in Figure 1.2: schlieren visualizes refractive index gradients and thus has a smooth variation from light to dark areas whereas shadowgraph visualizes the second derivative of refractive index and thus has sharp variations from light to dark at edges of the plume.

The modern retro-reflective shadowgraph system used for high speed imaging was developed in 1958 by H. E. Edgerton [4]. The system consists of a high intensity light source that is projected onto a retro-reflective screen. When a refractive object is placed in between the light and screen it distorts the path of the light casting a shadow of the object on the screen. This effect is shown in Figure 1.3. A camera placed near the light source is then able to record the image on the screen. The first documented use of this system was the imaging of the shock wave from a ”dynomite cap” [4]. This technique has been revived in recent works to be used again for explosive testing [5, 6]. The main advantage of the system is that it can be economically scaled up to a 2.5m by 2.5m test section. The larger test section allows for the study of refractive objects too large to be imaged with a traditional schlieren system, such as explosively driven fragments and firearms [3]. Increasing the size of the test section beyond this becomes technically challenging due to the need for a point light source in excess of 1 kilowatt and a retroreflective screen to provide the background. Larger systems have been demonstrated up to about 5 by 5m [7], but this can be challenging to illuminate

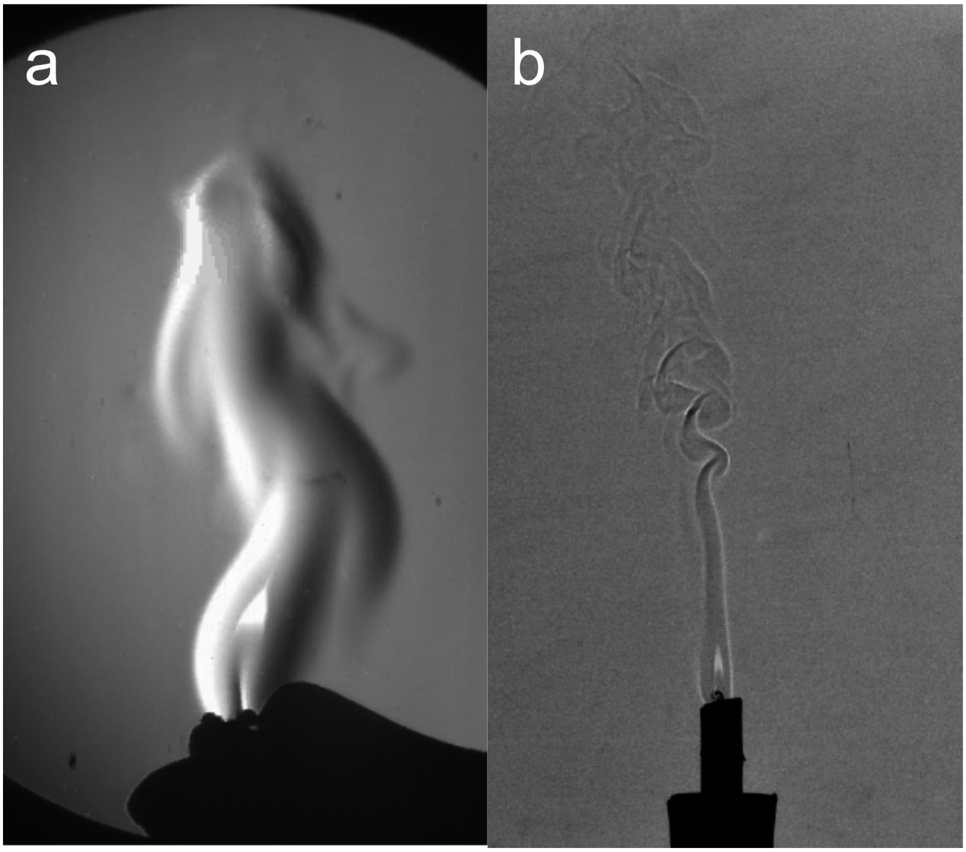

Figure 1.2: (a) Schlieren image of a lighter utilizing a vertical knife edge. (b) Retro-reflective shadowgraph of a candle.

with microsecond exposures. In addition all components of the system can be easily damaged by explosive fragments. This fragility and the limited test section size, limit the explosive articles that can be imaged within a shadowgraph system without damaging components.

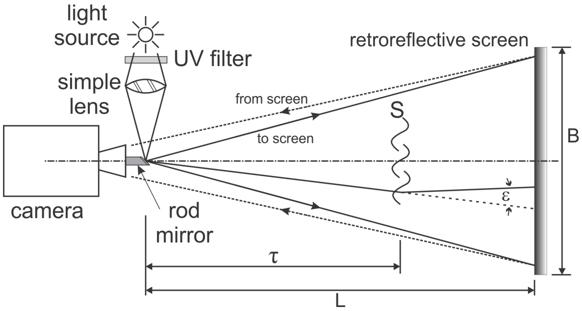

Figure 1.3: Diagram of rod mirror retro-reflective shadowgraph system with light ray paths shown.

1.2.3 Background Oriented Schlieren

Background oriented schlieren (BOS) is a modern refractive imaging technique that visualizes refractive objects via their distortion of a distant background [8]. BOS has a lower resolution and sensitivity than schlieren or shadowgraph but has no limitation on the area it can image. The phenomenon that BOS utilizes was first noticed by Schardin in 1942 but was not until 60 years later that the digital imaging and image processing technology ideal for the modern technique was commonly available [3, 9]. The modern BOS technique was simultaneously developed by Dalziel et al. [10] and Meier [11] in 1998-1999.

An advantage of BOS systems are their simplicity in setup. The two requirements for a BOS system are a camera at a fixed location and a background opposite the camera. BOS systems typically utilize a speckled background to provide the high contrast and spatial frequency needed. The speckle pattern was either applied with dye or paint or projected with a laser system [8]. It was later shown by Raffel et al. [12], Kindler et al. [13], and Hargather et al. [14] that many naturally occurring landscapes contain sufficient spatial frequency to be used as a background for BOS images. The camera is used to record a reference image of the background, then a refractive object is then placed in the field of view of the camera as is shown in Figure 1.4. The location of the object is an important factor in the sensitivity of the BOS system. The sensitivity of the system is defined as the minimum angle ϵ, in Figure 1.4, or the smallest density gradient the camera is able to detect [14, 15]. The exact sensitivity can be calculated using Equation 1.1:

$$\epsilon = d/(L-\tau) \tag{1.1}$$

in which ϵ is the sensitivity or smallest angle of refraction the system can detect, d is the apparent feature shift, L is the distance from the background to camera and τ is the distance from the refractive object to the camera [2, 16]. The sensitivity of a BOS system can be generally improved by minimizing the ratio τ/L while keeping the object and background in clear focus [2]. In practice it has been found that a $\tau/L = 0.5$ gives the optimum sensitivity and performance [15]. With the object in the field of view, the camera records a second image. The density variation within the field of view will cause the apparent location of features in the background to shift.

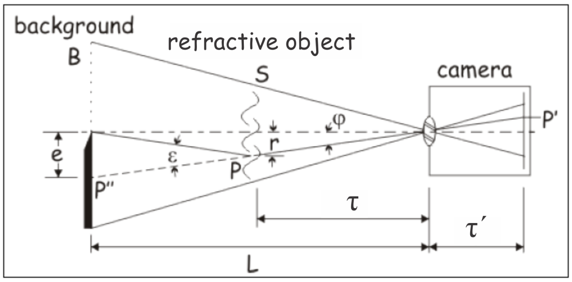

Figure 1.4: Diagram of typical BOS system with light ray paths shown.

There are multiple methods that can be used to detect and quantify the background shift between the two images and generate BOS images. The first method used to process BOS images uses particle image velocimetry (PIV) algorithms [8, 17]. PIV programs use cross correlation algorithms to detect and quantify the movement of tracer particles between images. From an image processing standpoint PIV processing is equivalent to BOS processing. For this reason PIV programs can be used to process BOS images with little to no modifications [18]. This method produces BOS images that show the shape and structure of the refractive object as well as quantify the direction and magnitude of the pixel displacement and is optically equivalent to a schlieren image [13]. The cross correlation method does have inherent drawbacks such as a reduction in resolution and high computational time.

A later developed method for BOS processing is image subtraction. Image subtraction compares the pixel intensities between the two images to detect refractive disturbances [14]. This method has higher resolution and lower computational time than the cross correlation method because it is performed on a pixel-by-pixel basis, but is unable to determine the magnitude or direction of the pixel displacement. BOS image subtraction was first used to study explosive shock waves in 2008 by Sommersel et al. [19]. The BOS image subtraction process was then improved for shock wave detection by Mizukaki et al. [20], and Hargather et al. [14]. This technique has be used to study explosive shock waves from charges ranging from 10^{-3} kg to 10^{3} kg [14].

1.3 Three-Dimensional Feature Reconstruction

Three-dimensional reconstruction combines information from two-dimensional images to determine the position of features in three-dimensional space. The origin of this technique is stereoscopy, which was developed in the mid nineteenth century [21]. Stereoscopy relies on the human brain to merge two slightly different flat images into a single three dimensional image. Each eye is shown a slightly different image with a stereoscope and the brain uses the difference in perspective to determine the distance to the object. This technique has mainly been used in entertainment and is still used in modern movie theater 3D glasses. A major military application of stereograms was in analysis of surveillance photographs [22]. This changed with the advent of modern computing technology [23].

Volumetric pair-wise feature matching uses matched features within stereograms and determines their location in three-dimensional space [24]. This technique was developed in 1976 by Marr and was largely based on how the human brain was thought to processes stereograms [23]. A modern iteration of the method begins by using a geometric camera calibration to determine the intrinsic and extrinsic parameters of the cameras [25]. Intrinsic camera parameters are those which are specific to each camera system, such as lens distortion and pixel size, while extrinsic parameters relate two camera systems. The camera calibration algorithm uses matched images of a calibration target with known dimensions, such as a checker board pattern, to determine the internal optical characteristics of each camera as well as the three-dimensional position and rotation of the cameras relative to each other [26]. The reconstruction method then finds a large number of unique points in each image [27]. A feature matching algorithm then finds matched points between the stereograms and using the camera parameters determines each point's location in three-dimensional space [25]. The resulting output is a list of points in three-dimensional space that define the scene. This method works well for finding and tracking unique objects in the cameras' shared field of view. This technique has been used to track ballistic objects and explosive fragments. When used with refractive imaging this technique can track the location of individual refractive objects but cannot define the objects' three-dimensional shape [28].

Using the volumetric visual hulls method the three-dimensional shape and structure of refractive objects can be determined. Tomographic BOS was first proposed in 2000 by Raffel et al. [12] and then demonstrated three years later by Klinge et al. [28]. The technique used a stereographic BOS system to detect vortices and then used volumetric feature matching to determine their three-dimensional location. This idea was expanded on by Atcheson et al. to use the visual hull method to reconstruct entire flow fields [29]. Visual hull reconstruction, first described by Martin et al., breaks each camera view into two regions, one containing the object and the other the background [30]. The areas describing the object in each camera view is then projected into three-dimensional space so that their intersections form a hull [24]. The resulting inferred visual hull is an approximation that contains the original object. The greater the number of views used to generate the hull, the better it approximates the original object. It was later shown that the visual hull method could be used to reconstruct the flow field of gas jets [29, 31, 32]. To date, the visual hull method has not been applied to reconstruction of explosive shock waves.

1.4 Shock Wave Propagation in Air

The scaled time radius curve of a shock wave is a fundamental property of an explosive material. The idea that explosive effects scale with the cube root of explosive mass dates to 1915 [33]. Thirty years later in 1944 this idea was expanded by Sachs to include effects of atmospheric conditions [34]. The Sachs' scaling equations are defined as:

$$R_s = \frac{R}{S} \tag{1.2}$$

$$t_s = \frac{ct}{S} \tag{1.3}$$

$$S = (\frac{W_0}{W})^{\frac{1}{3}}(\frac{101.325}{P_{atm}})^{\frac{1}{3}} \tag{1.4}$$

$$c = (\frac{T}{288.16})^{\frac{1}{2}} \tag{1.5}$$

where T is the atmospheric temperature in Kelvin, P_{atm} is atmospheric pressure in kPa, W is the mass of an explosive article and W_0 is the reference mass. These are used to determine the scaling factors S and c [35]. These scaling factors can be used to estimate an explosive's effects, such as the shock radius R_s and time t_s, from a single reference test. Sachs' scaling has been shown to hold over a wide range of explosive masses ranging from 10^{-6} kg to 10^{6} kg [35]. This scaling also allows the influence of atmospheric conditions to be removed so tests can be reported at standard temperature and pressure (STP, $P_{atm} = 1\ atm, T = 298\ K$).

An important characteristic of an explosive is the time radius curve of the shock wave. Historically this profile has been reported graphically or as a large table. In 1971 Dewey proposed using the least squares method to fit the radius of a shock wave to a parametric equation [36]. This empirically derived equation was written so that the shock wave would have a defined initial radius A and its velocity would decay to a defined velocity B at infinite time. The modern version of the equation, given by:

$$R_s = A + Ba_0t_s + Cln(1 + a_0t_s) + D\sqrt{ln(1 + a_0t_s)} \tag{1.6}$$

is written so that by setting B = 1, the shock wave decays to the speed of sound in ambient conditions, a_0 [37]. The parameters A, C, and D are determined by fitting the shock radius time data to the equation using a non-linear regression [35]. When reporting these parameters it is important to also report the range over which they were determined. This is done to prevent extrapolating the data into areas where it may not be valid, as with this multi-parameter curve fit, non-physical results are easily found outside the range of data. An advantage of this method is that the Dewey equation can be differentiated, with respect to time to:

$$\frac{dR_s}{dt_s} = Ba_0 + \frac{Ca_0}{1 + a_0 t_s} + \frac{Da_0}{2(1 + a_0 t_s)\sqrt{ln(1 + a_0 t_s)}} \tag{1.7}$$

This equation can be used to plot Mach number as a function of radius by parametrically varying time in the two equations.

The overpressure across a shock wave is given by:

$$\frac{P_2}{P_1} = \frac{2\gamma(M^2 - 1)}{\gamma + 1} \tag{1.8}$$

where γ is the ratio of the specific heats for the gas in which the shock is propagating, P_1 is the atmospheric pressure, P_2 is the absolute pressure after the shock wave, and M is the normal Mach number of the shock wave [38].

If the shock wave reflects from a rigid surface the overpressure is increased above this baseline. Shock wave reflections can be categorized into 3 groups: normal, oblique, and Mach reflections. A normal reflection is caused when a shock wave impinges on a surface that is perpendicular to its direction of travel. A second reflected shock is then formed and propagates opposite the original direction of travel. The overpressure generated by these two shock waves is given by:

$$\frac{P_{over}}{P_{atm}} = \frac{[(3\gamma - 1)M^2 - 2(\gamma - 1)][2\gamma M^2 - (\gamma - 1)]}{(\gamma^2 - 1)M^2 + 2(\gamma + 1)} \tag{1.9}$$

[38]. An oblique shock reflection is caused by a shock impinging on a surface at an angle less than perpendicular. The overpressure generated by an oblique reflection can be simply determined but requires knowing the Mach number of the incident and reflected shock [38]. When a shock wave impinges on a surface at a grazing angle it can form a Mach reflection. The conditions for Mach reflections are outside the scope of this work but discussion of the topic can be found in [39].

All of these reflection types can be observed when a charge is detonated offset from a flat surface. When the explosive shock wave first reaches the surface it will cause a normal reflection. This point will experience the highest overpressure on the surface. As the shock wave expands the reflection will become an oblique reflection. As the shock continues to expand the reflection type can transition to a Mach reflection. Because the highest overpressure will be generated by a normal reflection it is desirable to estimate the normal reflection overpressure at any point, which can be calculated with Equation 1.9 by knowing the Mach number. Thus by knowing the shock Mach number throughout a field the overpressure and normal reflected overpressure at any location can be determined.

1.5 Goals of Current Research

The present research is focused on developing a set of techniques that can be used to study the three-dimensional shock wave propagation from explosive tests. As discussed above, previous research has been limited to one or two-dimensional analysis, which assumed a large degree of symmetry. To expand on this prior work, the goals of this research can be summarized as:

- Develop an automated approach to detect shock wave locations in background oriented schlieren (BOS) images
- Characterize the three-dimensional shape of explosively driven shock waves
- Generate time resolved three dimensional reconstructions of shock wave propagation

CHAPTER 2

EXPERIMENTAL METHODS

A test series was conducted at the Energetic Materials Research and Testing Center at the New Mexico Institute of Mining and Technology to investigate shock propagation from explosions. Four individual field experiments were performed, each imaged with a multiple camera BOS system to allow reconstruction of shock wave propagation in three-dimensions.

2.1 Experimental Setup

The explosive charges used to generate the shock waves were 113 g (0.25 lb) C4 initiated with an RP-83 detonator. The details of each test are listed in Table 2.1. The components of each charge were assembled and affixed to a wooden table located in the middle of the open test pad. Figure 2.1 shows the steel fragmentation disk used in test 2 and 3 and how it was assembled into the explosive article. The detonator was triggered by an FS-17 fire set. The fire set sent a simultaneous signal to a Stanford Research Systems delay/pulse generator, which then sent a common TTL trigger signal to each of the high speed cameras.

Four high speed cameras were used in the test series and their locations are shown in Figure 2.2 and given in Tables 2.2 and 2.3. Figure 2.3 shows how the coordinate system used to describe the camera locations is defined relative to the master camera. The cameras were arranged in two configurations, configuration A had spread the cameras over a wider range of angles to provide more diverse views of the bare explosive while configuration B had the cameras closer together to better image the fragment producing shots. Two Phantom V711s were placed at a similar elevation to the explosive charge and were labeled as ″master″ and ″camera 2″. These cameras recorded images with a resolution of 912x704 pixels. Two Photron SA-X2s were placed at elevated positions and were labeled cameras 3 and 4, respectively. The SA-X2s recorded images at 1024x1024 pixels. All cameras recorded at 10,000 frames per second (fps). The exposure of each camera was set to provide well balanced images and ranged from 3 μs to 6.3 μs. Each camera was supplied with an IRIG timing signal for time stamp and synchronization.

To delay ground shock reflections, the charges were elevated 0.9 meters (3 feet) from the ground by small wooden tables. A plywood wall was constructed to allow visualization of shock wave reflections from a rigid surface in the field of view. The plywood reflecting wall was 1.2 meters wide by 2.4 meters tall (4 feet by 8 feet) and was placed between 1.37 meters (54 inches) and 4.5 meters (15 feet) from the charge. Two pencil style pressure probes, PCB Model 137B2XB, were place on either side of the reflection wall and equidistant to the charge as the reflection wall.

Figure 2.1: (a) The steel fragmentation disk comprised of 31 hexagonal steel fragments secured within a ring used in tests 2 and 3. (b-c) The explosive configuration used in tests 2 and 3. The steel fragmentation disk is opposite the detonator. The article is held in a foam stand and the entire assembly is secured to the table with tape. Tests 1 and 4 had the same arrangement of the explosive, detonator, and foam mounting.

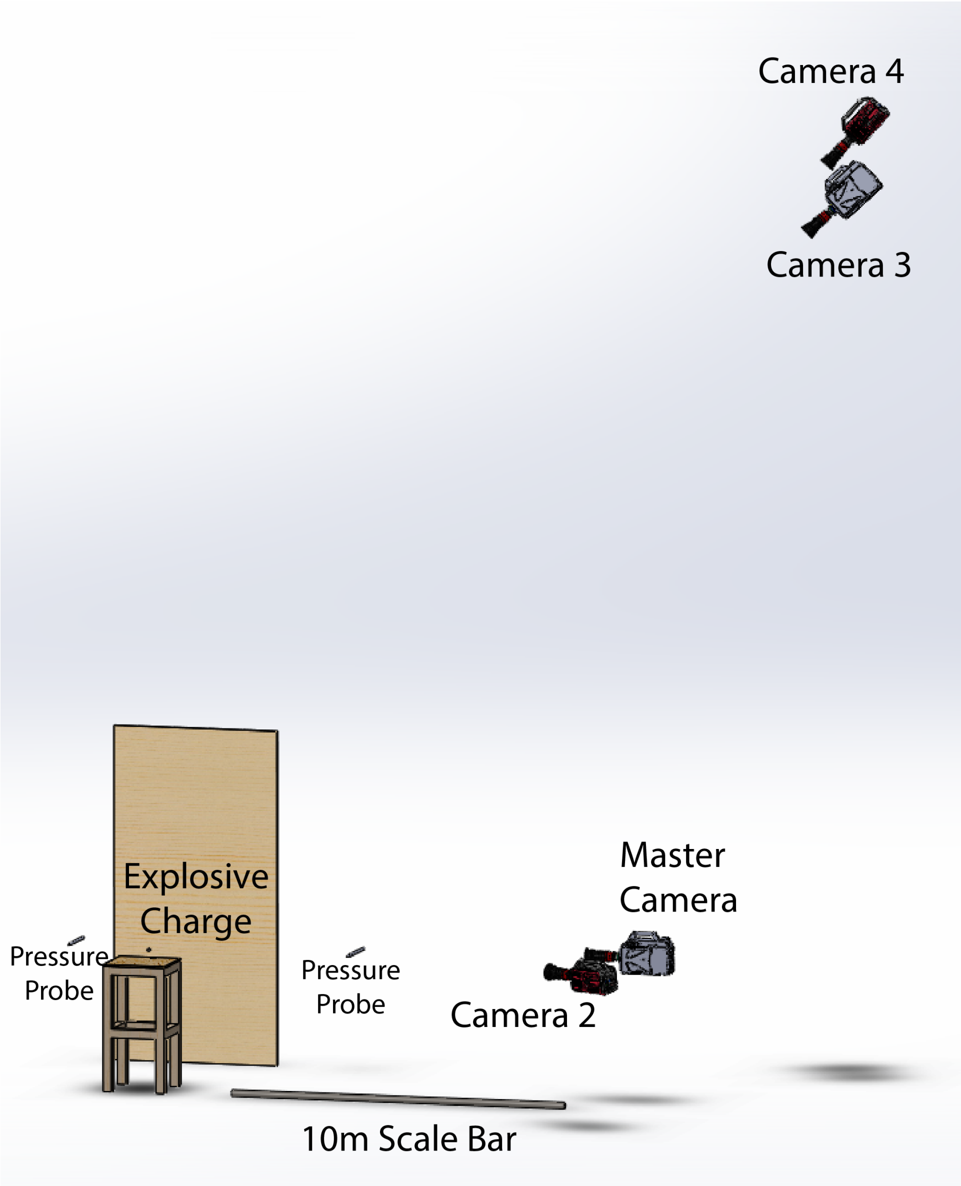

Figure 2.2: Diagram of camera configuration A. Shown are the high speed cameras and the charge table with the reflection wall behind it. The pencil style pressure probes are on either side of the reflection wall. The cameras, pressure probes, explosive charge and reflecting wall are at scale but the distances between items is shown at quarter scale. A 10 meter scale bar is shown at the bottom at the quarter scale.

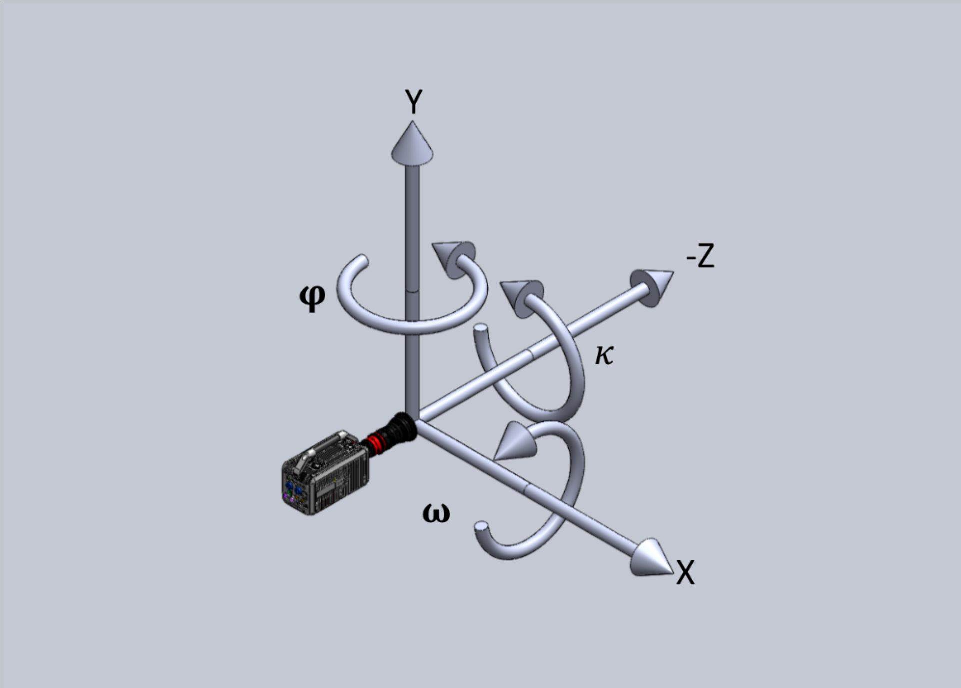

Figure 2.3: Diagram of the coordinate system that the stereo camera calibration algorithm uses to define the location and rotation of the cameras. The camera shown is the master camera, which is located at the origin of the coordinate system. The coordinate system in this work used a 1-2-3 (or x-y-z) rotation matrix.

Table 2.1: Summary of tests series.

Test Number	Charge	Charge Configuration	Camera Configuration
1	113 g C4	Bare Charge	A
2	113 g C4	Steel Fragment Disk	B
3	113 g C4	Steel Fragment Disk	B
4	113 g C4	Acrylic Fragment Sheet	B

Table 2.2: Summary of camera relative position for camera setup A.

Camera	X position (m)	Y position (m)	Z position (m)	ω (degree)	φ (degree)	κ (degree)
Master	0	0	0	0	0	0
2	−4.9 ±0.1	0.1 ±0.03	4.5 ±0.2	−3.2 ±0.4	−18.2 ±0.7	2.1 ±0.1
3	7.2 ±0.5	7.2 ±0.5	22.4 ±0.5	−5.9 ±1.0	33.5 ±1.5	−4.0 ±0.4
4	7.7 ±0.2	4.2 ±0.3	21.2 ±0.3	−14.1 ±0.8	35.4 ±0.4	−1.6 ±0.3

Table 2.3: Summary of camera relative position for camera configuration B.

Camera	X position (m)	Y position (m)	Z position (m)	ω (degree)	φ (degree)	κ (degree)
Master	0	0	0	0	0	0
2	−5.8 ±0.1	−0.1 ±0.01	0.4 ±0.1	−1.4 ±0.3	−22.9 ±0.2	4.1 ±0.1
3	−4.8 ±0.1	5.1 ±0.2	18.7 ±0.2	−12.6 ±0.4	−26.1 ±0.4	7.1 ±0.2
4	−4.3 ±0.1	5.7 ±0.1	12.2 ±0.3	−7.6 ±0.4	−9.3 ±0.4	0.7 ±0.1

2.2 Synchronizing

A source of error when performing multi-camera reconstructions is the difference in time between when each camera starts to record an image. The process of configuring the cameras to take images simultaneously is referred to as camera frame synchronization. Phantom and Photron high speed cameras have an internal system to synchronize multiple cameras. This system works by the user selecting a master camera. The master camera uses an internal crystal oscillator to generate the desired frame rate. The internal signal is used to drive the master's frame cycle. The internal signal is also converted to a "frame sync clock pulse", which is supplied to an external port. This TTL pulse signal is high when the master camera's digital shutter is open. The signal goes low when the master camera finishes recording its image. This signal is sent to the other cameras via a Bayonet Neill-Concelman (BNC) cable. The other cameras match opening their digital shutter to the start of the TTL signal. The result is all cameras' digital shutters opening at the same instant and closing based on their own exposure time. This system works well but has multiple limitations. The maximum distance between the two furthest cameras must be under 10 meters (33 feet) [40]. This may not be a problem in a laboratory setting but field testing often utilizes much larger camera separation. The system also cannot synchronize more than four cameras [40]. Most commercial high speed camera manufacturers have a system like this in their cameras. Despite this it can be difficult to synchronize cameras across different manufacturers.

There are few options if using the on-board camera synchronization system is not possible. The simplest option is to not synchronize the cameras. Each camera will uses its own internal oscillator to determine when it opens its digital shutter. The camera will then close its shutter based on its exposure setting. This results in an unknown frame delay between cameras, even with a common trigger signal. The maximum of this delay is the inverse of the frame rate. At 10,000 fps the maximum possible delay is 100 μs. This was determined to be an unacceptable amount of error for this test series.

A more technically challenging synchronizing method is to supply each camera with a independently generated timing signal. This method uses a pulse generator to make the desired timing signal. Cables of equal length are then used to supply the signal to the cameras. The initial signal must be quite strong since the signal is being divided among several cameras. For this reason a signal amplifier might be required. This method will result in frame delays at or below that of the manufacturer's method. It will also allow for greater separations between cameras. The added equipment and possible complications made this method too challenging for this test series.

The method chosen for this test series was to use inter-Range Instrumentation Group time codes (IRIG time codes) to synchronize the cameras. This method utilizes a IRIG receiver/clock to obtain precise time from an outside source. The IRIG receiver then supplies a timing signal to each of the cameras. Each camera then uses the timing signal to select when it opens its digital shutter.

Table 2.4: List of the IRIG time at which first light is recorded by each camera. The time recorded by each camera within a test was identical to the millisecond so only the microsecond portion of the time stamp is reported.

Camera:	Test 1 (μs)	Test 2 (μs)	Test 3 (μs)	Test 4(μs)
Master	704	104	904	107
2	707	107	907	104
3	703	166	853	092
4	713	135	909	139

The timing signal can also be used to stamp a time code to the images. The IRIG time first light from the explosion was recorded by each camera from each test is listed in Table 2.4. The maximum difference in time between the cameras within a test was 62 μs. This method reduces the delay over un-synchronized cameras without the added complexity of using a signal generator.

2.3 Camera Calibration Techniques

Camera calibration is used to relate the images taken with a digital camera to the physical objects they record. There are two types of camera calibration used in this work: single camera calibration and stereo camera calibration. Single camera calibration techniques are used to determine the size of refractive objects in BOS images. Stereo camera calibration techniques are used to determine the position and orientation of cameras relative to each other, and the three-dimensional reconstruction of the shock propagation. Both single and stereo camera calibration can be calculated by analyzing images of checker board patterns, which is shown in Figure 2.4.

Single camera calibration techniques allow for measurements to be made in a single plane. A MATLAB script was written to preform these calibrations. This script analyzed images of a checkerboard pattern similar to Figure 2.4. The dimensions of the checkerboard pattern were entered and the corners of the checkerboard pattern automatically detected. The algorithm then determined a pixel per length calibration value for each pair of corners. The statistical frequency of the calibration values were determined and plotted. If the calibration board was tilted out of the correct plane the distribution of calibration values would skew. As a result only frames that produced a normal distribution of calibration values were accepted. Figure 2.5 shows a plot of statistical frequency of the calibration values that was acceptably close to a normal distribution. The statistical characteristics of each camera calibration were calculated and are listed in Tables 2.5 and 2.6. The mean calibration value is used to make measurements within the plane the calibration was taken; two standard deviations from the mean was used as the uncertainty in each calibration value.

Figure 2.4: Image of checker board with 5 inch squares used to generate single and stereo camera calibrations.

A single camera is not able to determine the distance between the camera and a plane. Thus, it is not possible to correct measurements for perspective shifts due to a changing measurement plane. In this BOS system the shock wave is assumed to be imaged in a fixed plane. Since the background is sufficiently far behind the object, the diffuse light coming from the background was assumed to be effectively parallel and thus the shock wave is visualized in a single plane that is perpendicular to the camera axis that contains the shock source. For this reason the system is calibrated in the plane that contains the shock source.

Table 2.5: The statistical characteristics of calibration values found for camera configuration A.

	Master	Camera 2	Camera 3	Camera 4
Mean (pix/mm)	0.1115	0.0815	0.1140	0.1102
Median (pix/mm)	0.1118	0.0815	0.1141	0.1102
Minimum (pix/mm)	0.1073	0.0796	0.1124	0.1092
Maximum (pix/mm)	0.1148	0.0838	0.1155	0.1114
Standard Deviation (pix/mm)	0.0015	0.0009	0.0006	0.0004

Table 2.6: The statistical characteristics of calibration values found for camera configuration B.

	Master	Camera 2	Camera 3	Camera 4
Mean (pix/mm)	0.1067	0.1448	0.1099	0.1194
Median (pix/mm)	0.1068	0.1445	0.1100	0.1193
Minimum (pix/mm)	0.1046	0.1378	0.1077	0.1182
Maximum (pix/mm)	0.1088	0.1574	0.1119	0.1209
Standard Deviation (pix/mm)	0.0008	0.0024	0.0008	0.0006

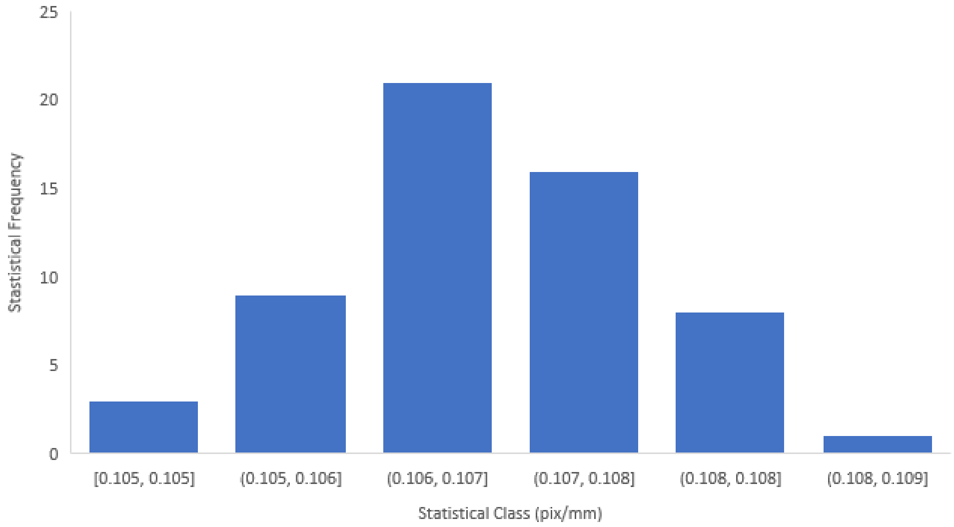

Figure 2.5: The statistical frequency of calibration values from the Master camera in configuration B.

Stereo camera calibration techniques are used to determine the internal and external parameters of 2 cameras in an imaging system. In this work stereo camera calibrations were processed by MATLAB's Stereo Camera Calibrator [25]. An example calibration is shown in Figure 2.6. This method required two cameras to image a checkerboard pattern simultaneously as it is moved and rotated through the shared field of view of the cameras. One frame used for calibration is shown in Figure 2.4. The algorithm extracts the position of the corners of the squares in the checker board pattern in each frame. It then compares the location of the squares in each camera's field of view with the known size of the squares. This data is then processed into a series of parameters and uncertainties that describes the translation and rotation from one camera to the other [25]. The translation between cameras is given as a 3 element matrix from camera 1 to camera 2 in the units used to define the checkerboard pattern. The rotation of camera 2 relative to camera 1 is given as a 1-2-3 rotation matrix of size 3-by-3. The Euler angles can be extracted from the rotation matrix by using:

$$m_{11} = cos\varphi cos\kappa \tag{2.1}$$

$$m_{12} = sin\omega sin\varphi cos\kappa - cos\omega sin\kappa \tag{2.2}$$

$$m_{13} = cos\omega sin\varphi cos\kappa + sin\omega sin\kappa \tag{2.3}$$

$$m_{21} = cos\varphi sin\kappa \tag{2.4}$$

$$m_{22} = sin\omega sin\varphi sin\kappa + cos\omega cos\kappa \tag{2.5}$$

$$m_{23} = cos\omega sin\varphi sin\kappa - sin\omega cos\kappa \tag{2.6}$$

$$m_{31} = -sin\varphi \tag{2.7}$$

$$m_{32} = sin\omega cos\varphi \tag{2.8}$$

$$m_{33} = cos\omega cos\varphi \tag{2.9}$$

where ω, φ, and κ are the elementary rotations around the x, y, and z axis respectively, and m_{ab} is the matrix value at location (a, b) [26].

The MATLAB Stereo Camera Calibrator can be used to calibrate a group of more than 2 camera but not in a single operation. To calibrate a large group of cameras, the cameras must share a field of view. The camera with the most common view is selected as the master camera. A series of calibrations is then run between the master camera and the remaining cameras one at a time. This produces a series of parameters, which are listed in Tables 2.2 and 2.3, which describe the location and rotation of the cameras with respect to the master camera.

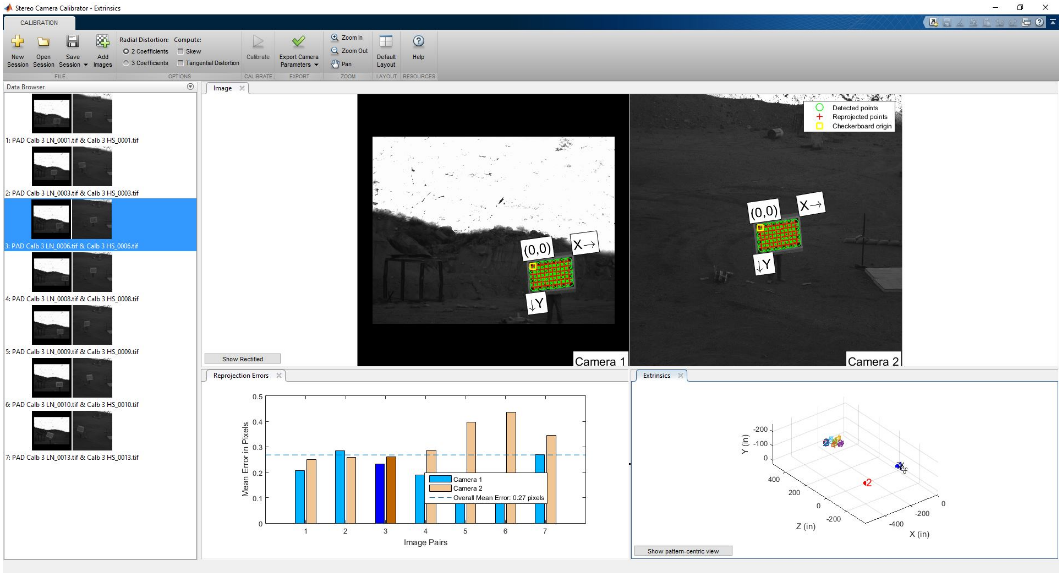

Radial Distortion: ● 2 Coefficients ○ 3 Coefficients

Compute: ☐ Skew ☐ Tangential Distortion

1: PAD Calb 3 LN_0001.tif & Calb 3 HS_0001.tif
2: PAD Calb 3 LN_0003.tif & Calb 3 HS_0003.tif
3: PAD Calb 3 LN_0006.tif & Calb 3 HS_0006.tif
4: PAD Calb 3 LN_0008.tif & Calb 3 HS_0008.tif
5: PAD Calb 3 LN_0009.tif & Calb 3 HS_0009.tif
6: PAD Calb 3 LN_0010.tif & Calb 3 HS_0010.tif
7: PAD Calb 3 LN_0013.tif & Calb 3 HS_0013.tif

Figure 2.6: Example calibration using MATLAB's stereo camera calibrator. The image pairs used to generate the calibration are shown in the left. An example image is shown center where the checker board pattern has been detected in the image pair. Bottom center displays the mean projection error for each image pair. Bottom right shows the calculated camera locations.

2.4 BOS Image Processing

When a refractive object, such as a shock wave, is in a field of view it distorts the appearance of the background. If a digital camera records an image before and after the refractive object is in view it will record the background distortion. If the background is a random pattern of appropriate size, the distortion will be recorded as a change in the pixel intensities. The distortion can be difficult to detect by the human eye. Figure 2.7 a and b are images recorded without and with a shock wave in the field of view. The images are processed using BOS image subtraction techniques here to identify the shock wave locations.

The BOS processing technique of image subtraction is used to improve detection of refractive objects. In this work, the technique is used to compare two images from a static camera at different times. The two images selected will be a reference image, referred to as a cold image, and the image which is being analyzed, or hot image. In the image subtraction process used, the values of the pixels in the cold images are compared on a pixel-by-pixel basis from the pixel values from the hot images:

$$pic(x,y) = \frac{[hot(x,y) - cold(x,y)]^2}{\frac{hot(x,y)+cold(x,y)}{2} + 1} \tag{2.10}$$

where $hot(x,y)$ is the value of a pixel at location x,y in the analyzed image, $cold(x,y)$ is the value of a pixel at the same location in the reference image, and $pic(x,y)$ is the value recorded for that pixel location in the new image [15]. Any pixels which have not changed between the two images will result in a value of 0 or a black pixel in the new image. The value of any pixel change will be used to determine the brightness of the pixel in the new image. The greater the resulting value, the brighter the pixel will be in the new image. When imaging refractive objects, the magnitude of change in pixel values tends to be small. The resulting image has too low contrast to be visible. Histogram stretching is manually performed on each image to make the shock wave more visible. The values used in each histogram stretch is experimentally determined to produce an image with a clearly visible shock wave with minimal background noise.

The image subtraction method can be optimized for shock wave tracking by careful selection of the reference image. In traditional BOS, the reference image is taken before the event. The resulting image shows everything that has changed since detonation including the fireball, changes in lighting due to the fireball, lens glare, fragments, and the shock wave. Figure 2.7c is created by comparing an image during test to a pre-test image. In this image the shock wave is difficult to detect through the noise created by the flare of the fireball. One method to reduce this noise is to use the previous image as the reference image. This method, referred to as sequential image subtraction, shows only high velocity features such as fragments and shock waves that have changed in the time between frames and does not show slower objects such as the fireball. This method also increases the apparent density with which the shock wave is visualized. This makes detection of the shock easier without changing the location of the shock front. The difference made by selection of a proper reference frame can be seen in the difference between 2.7c and d. These images have been processed using the same method except that d used sequential subtraction.

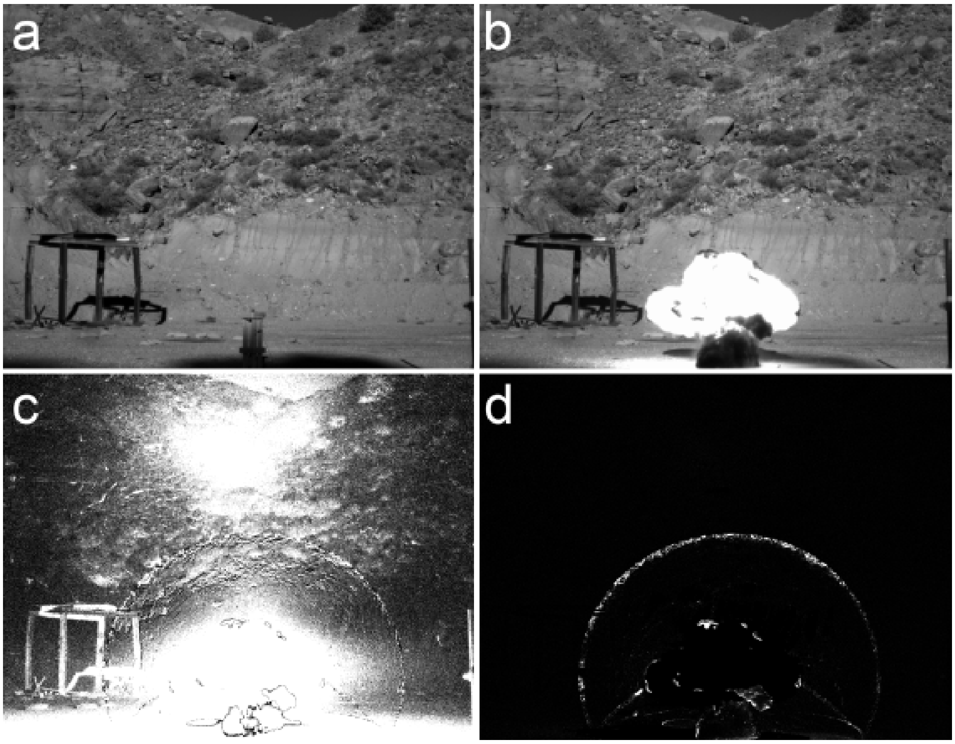

Figure 2.7: (a) Reference image before detonation. (b) Hot image 4 ms after detonation. (c) BOS image created by image subtracting (a) and (b). (d) BOS image created by image subtracting (b) and its previous high-speed frame, here recorded 0.1 ms earlier.

2.5 Reconstruction

A three-dimensional reconstruction of a shock wave can be generated from multiple two-dimensional refractive images. The first step in generating this reconstruction is to record a shock wave in multiple BOS systems. Each BOS system recorded a single plane of the shock wave. To record a sample set diverse enough to avoid bias the cameras should be spread out over a large arc, such as is shown in Figure 2.8. Once the shock wave has been recorded and processed into BOS images the location of the shock wave in each image must be determined. The process of detecting the shock wave location is covered in detail in Section 3.3. The shock wave locations must then be converted from pixel units to real units.

This conversion is done by dividing the pixel measurements by the pixels per length calibration value found for that camera. At this point each camera has generated a single plane reconstruction of the shock wave. This plane is centered at the shock wave source and perpendicular to the camera. The angles between the planes visualized by each camera is equal to the angles between the cameras, which is measured by the stereo camera calibration and reported as a rotation matrix. This is shown as a two dimensional schematic in Figure 2.8. The single plane reconstruction is rotated about the shock wave source by multiplying the matrix of shock wave locations by the rotation matrix. This shifts each two dimensional reconstruction into three dimensions. The shock locations from each camera are then combined into a single three dimensional reconstruction. This is done by overlaying the points from each reconstruction into a single point cloud. A surface can then be fit to the point cloud. In this work, the surface was calculated to be a sphere using an open source MATLAB script [41]. This process is then repeated for each frame recorded of the shock wave expansion for the bare charge in Test 1. Tests 2-4 are not fit with any surface as significant asymmetries in the shock surface were identified due to the fragments included in the blast.

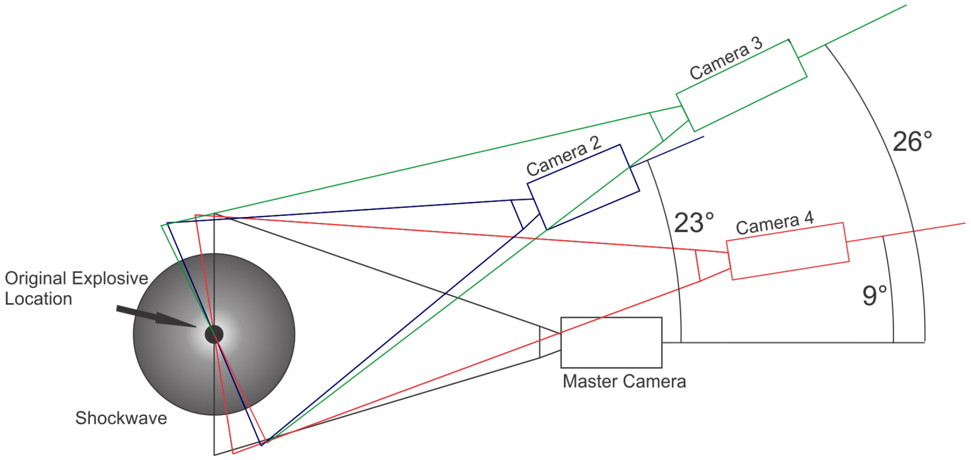

Figure 2.8: Schematic of the angles at which the cameras view the shock wave and the planes in which the shock wave is visualized for camera orientation B.

CHAPTER 3

AUTOMATED SHOCK DETECTION

Once refractive images have been generated there are two methods to extract the location of the shock wave, manual and automated point detection. Manual point detection relies on a user to identify and select the location of a feature. This method can be quickly implemented but is impractical for large data sets. Automated point detection uses an understanding of the underlying physics to identify the location of the shock in each frame. Automated point detection is able to process large data sets efficiently and effectively, and a routine for automated detection was developed and implemented here.

3.1 Manual Point Detection

Manual point detection employs a user and prior experience and knowledge to determine the location of a shock wave in an image. This method can be implemented quickly and required few lines of code. As a result it was used as a first approach to detect shock waves. A simple MATLAB routine was written to facilitate manual detection. In the routine, the user manually clicks on locations to be identified as the shock front. The largest problem is that it is a non-transferable method. Since the method relies on a user's prior experience and knowledge it cannot be transferred to a new user without training. Even after training there may be statistical bias between users. This method is also not efficient for processing large data sets due to the large time commitment required.

To study the reliability of manual detection, it was used to measure a circle of known size. A circle with a diameter of 7.62 cm (3 inch) was printed on paper and fixed rigidly in the field of view of a Phantom V711. An image of the circle was recorded and is shown in Figure 3.1. The camera was calibrated with the single camera calibration method and the manual detection script was used to select the edge of the circle at 37 points. The data was analyzed and the statistical characteristic of the measured radius and the difference between the measured radius and the true radius is listed in Table 3.1. The statical frequency plot of the data is given in Figure 3.2 and shows that the data does not fit a normal distribution. The mean error, in pixels plus one standard deviation, gives an uncertainty of 2 pixels in the measurement, which was used as a baseline against which the automated code was compared.

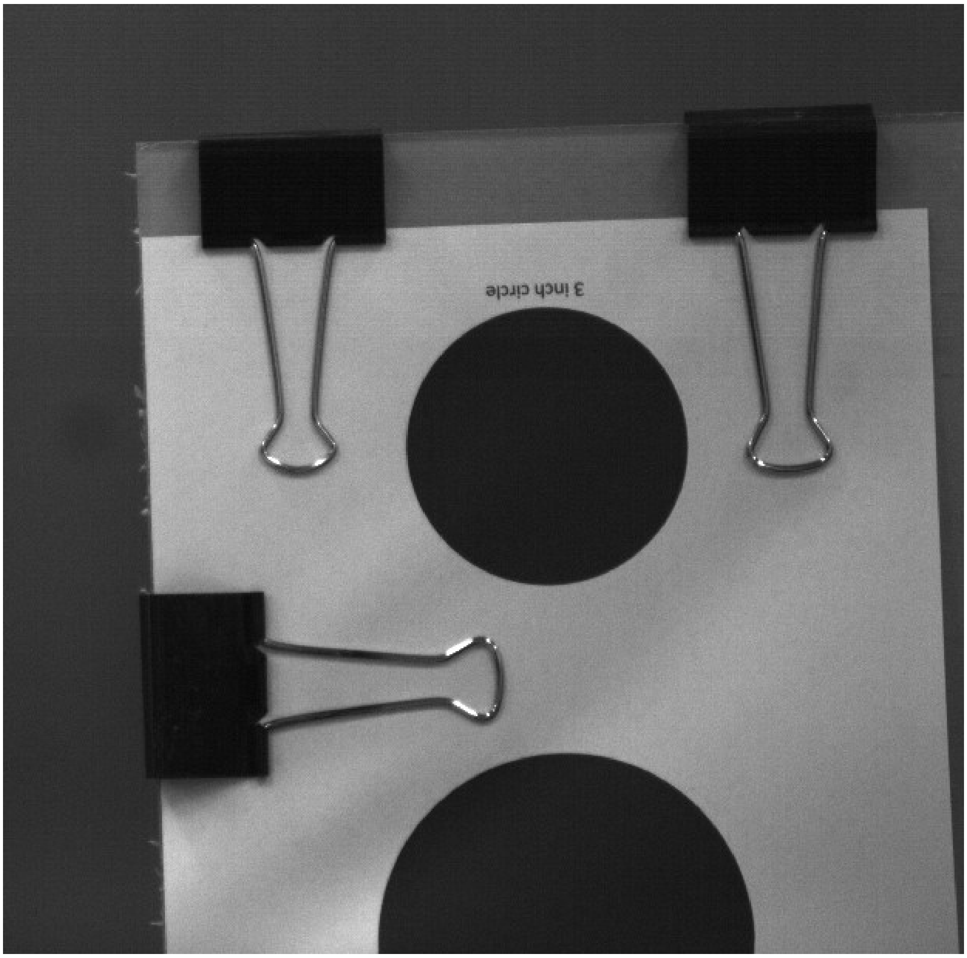

Figure 3.1: A circle, printed on copy paper, with a diameter of 7.62 cm (3 inch) and rigidly fixed in the field of view. This image was used to test the manual point detection.

Table 3.1: Statistical characteristics of manual detection data.

	Mean	Median	Minimum	Maximum	Standard Deviation
Measured Radius (cm)	3.82	3.82	3.71	3.96	0.07
Difference between measured and true (pixels)	0.33	0.14	-2.23	3.53	1.52

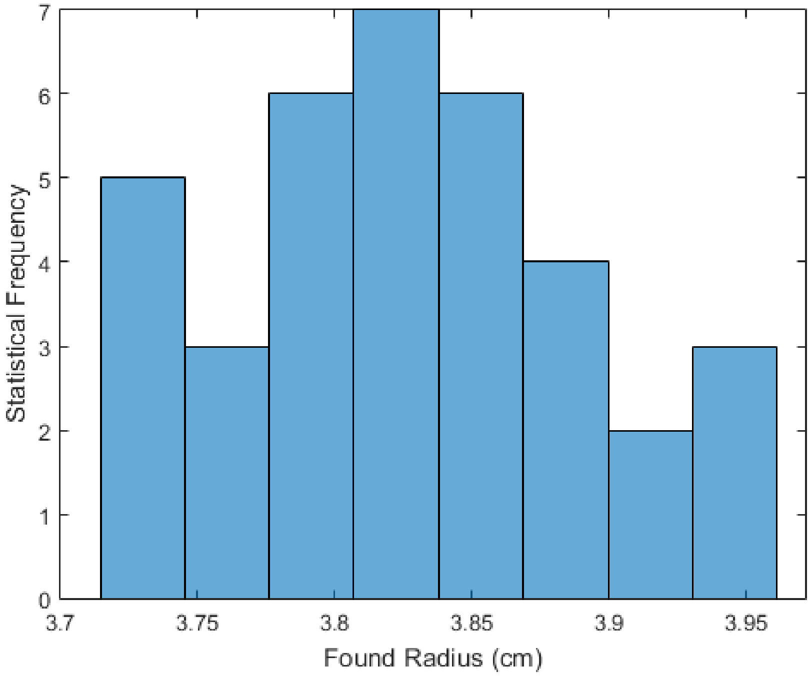

Figure 3.2: The statistical frequency of the radius values found with the manual detection method.

3.2 Criteria for Shock Wave Detection

Detection algorithms utilize a set of criteria to select the desired target from the background noise of an image. The selection criteria used to detect shock waves is derived from an understanding of the compressible flow that governs shock waves. Shock waves are discontinuities that separate high pressure, high particle velocity areas from undisturbed air [42]. From this definition the selection criteria can be derived. The uniform pressure differential across a shock wave causes it to expand radially. The implication of this is that an un-disturbed shock is a simple curve that can be described in polar coordinates using only a radius. Since a shock wave is a discontinuity entering undisturbed air its leading edge will be a step function. When imaged with a refractive imaging technique, such as BOS, the leading edge of the shock should be a crisp arc. Because the shock wave separates two distinct areas even after encountering obstacles the line describing a shock wave must remain continuous. This means that all sections of the leading shock wave must be connected.

These three criteria were used to build the algorithm to select shock waves in BOS images:

1. Shock waves sections will be a simple curve with only a singe radius, originating from a known point.

2. Shock front will be visualized as the leading edge of the distortion.
3. All segments of the primary shock will be connected.

3.3 Design of Automated Point Detection Algorithm

Using the established selection criteria an algorithm was written to efficiently search BOS images for shock waves. The primary basis of the algorithm was the first selection criteria, the shock wave will be a simple curve with a single radius. This was paired with the fact that in BOS images processed with the subtraction method of Equation 2.10, refractive objects are visualized as bright objects. The implication is that shock waves in BOS images will be a collection of bright pixels in a band of radii. To determine radius, the location of the shock wave source must first be identified. This is done by manually selecting the location of the explosive article in a pre-detonation image. To reduce processing time an initialization of the shock wave location is made. Using the initialization radius, search windows are generated for the search algorithm. Using the explosive location as the origin, the radius of each pixel within the search window is calculated. The pixel values are summed for each integer radius value. These data are then plotted as a histogram with the binned value on the Y axis and the radius on the X axis. The peak of this plot defined the radius with the highest brightness. Figure 3.3 shows that the peak occurs at the center of the shock structure. Differentiating the binned data, with a numerical backwards difference method, shows the two peaks where there is a dramatic change in brightness. The large positive peak indicates the location of the trailing edge of the shock wave and Figure 3.4 shows that the large negative peak indicates the location of the shock front.

Figure 3.3 demonstrates the search algorithm functionality for a setup with only five search zones. The algorithm breaks the overall shock wave arc into five equally spaced regions, each of which is shown with a yellow box. The algorithm sums the pixel intensities along each potential arc radius through the interrogation window. The shock wave center is identified as existing at the level with the maximum occurrence, and is then marked in each interrogation window by a single point with the red dot. Figure 3.4 uses this same process for thirty seven search zones but identifies the largest negative peak as the location of the shock front. This process is repeated in thirty seven search zones to generate Figure 3.5. This figure shows that the automated edge detection algorithm functions well and is able to reliably detect the location of the shock front. The automated edge detection algorithm is given in Appendix A.

To determine the accuracy of the automated detection algorithm it was compared to manual detection and found to have similar accuracy. To determine the true location of the shock wave in each image, a careful manual detection was conducted on a BOS image that clearly showed the shock. Special care was taken to ensure that the exact pixel was selected that contained the shock front. The

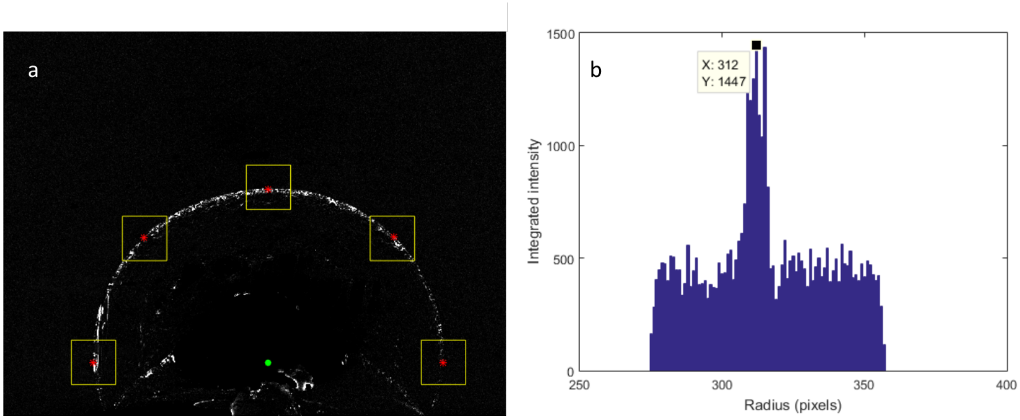

Figure 3.3: (a) Shows the features used in the automated detection algorithm. The green circle is located at the center of the shock wave. The yellow boxes are the search zones and the red dots are the shock location found in each search zone. (b) The histogram of intensities of the radius in the middle search box. The peak point is shown.

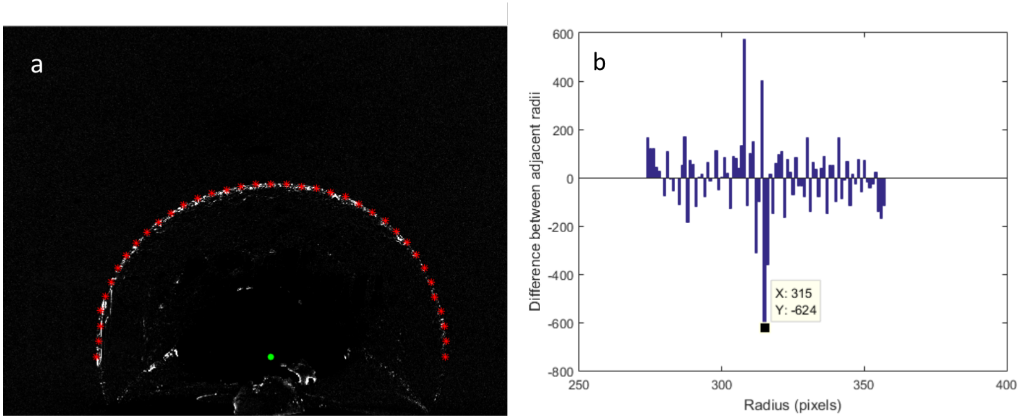

Figure 3.4: (a) The results of the improved automated detection algorithm. (b) A graph of the derivative of intensity radius data. The lowest point is shown and taken as the location of the shock front.

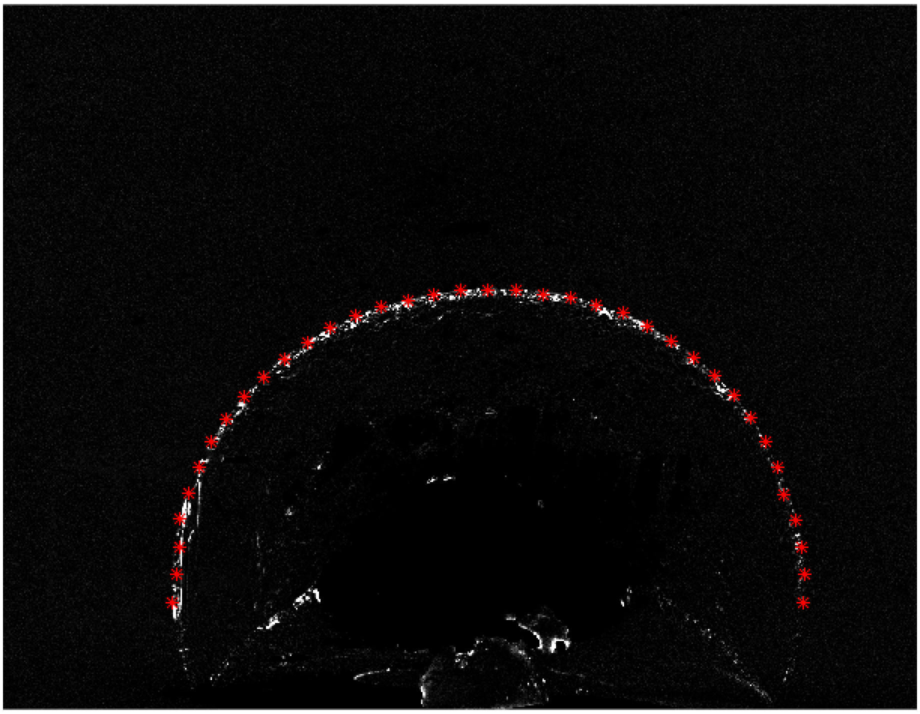

Figure 3.5: Image demonstrating the code's ability to detect the shock front, each red dot is a found location on the shock front.

time required to achieve this level of accuracy is impractical for analyzing multiple images, which is why it is specified from standard manual selection. The image was then processed using the automated shock detection algorithm and the locations compared. A set of locations found using the careful manual detection and the automated shock detection are shown in Figure 3.6. The difference between the locations are plotted in Figure 3.7 and the statistical characteristics of the difference is listed in Table 3.2. The mean error plus one standard deviation gives an uncertainty of 2.27 pixels, which is comparable to the uncertainty found for standard manual detection.

Table 3.2: Statistical characteristics of the difference in the locations found with the careful manual detection and the automated detection.

Mean (pix)	Median (pix)	Minimum (pix)	Maximum (pix)	Standard Deviation (pix)
0.71	0.39	-1.40	5.19	1.56

The image processing applied to BOS images prior to the automated detection algorithm affects the accuracy of the algorithm. One variable in the BOS image processing is the selection of a reference image. To study the effect that the choice of reference image has on the accuracy of the automated shock detection routine, five frame separations of n-2, n-3, n-4, n-5, and n-10, were selected in addition to the initial sequential step of n-1. The first four frame separations, of n-2, n-3, n-4, and n-5, were selected to image the shock waves with decreasing amounts of overlap. The final frame separation, of n-10, was selected to visualize the two shock waves with a clear separation between them. The frame at t=4.5ms from the master camera on Test 1 was processed into a series of BOS images using a reference image determined by the 6 frame separations. No other parameters, such as the values of the histogram stretch, were changed between images. The separation used to generate each image is listed at the top of Figure 3.8. The left most image shown in Figure 3.8 was generated using the sequential processing, which was used on the other BOS images within this work. The right most image of Figure 3.8 shows the shock at two times visualized similar to a traditional BOS process using a pre-event reference image. The shock is visualized as a broad gradient that is densest directly behind the shock wave to more sparse farther behind the shock. Comparing the furthest right and left images of Figure 3.8, the effects of sequential imaging can be seen. In the sequential BOS image, only a narrow but dense band is visualized from each image resulting in a uniformly dense band visualized behind the shock. As the frame separation is increased, moving from left to right in Figure 3.8, the shocks visualized from each image become more separated and therefore more distinct. As the frame separation increases, a larger band of each shock wave is visualized and the background noise increases.

The BOS images used to create Figure 3.8 were processed using the automated detection algorithm and the total uncertainty for that combination determined. The identified shock locations and total uncertainty for each time separation are listed in Figure 3.9. In each case the detection algorithm located one of the two shock fronts visualized from the two images. Which shock is detected is randomly distributed resulting from the non-uniform background. As the shock visualized from reference image moves away from the true shock front location the total uncertainty, or the mean error plus one standard deviation, increases. This can be seen in the n-2 through n-5 images from Figure 3.9. In the n-10 image from Figure 3.9 the shock wave visualized from the reference image is outside of the automated detection algorithm's search area and as a result is not detected.

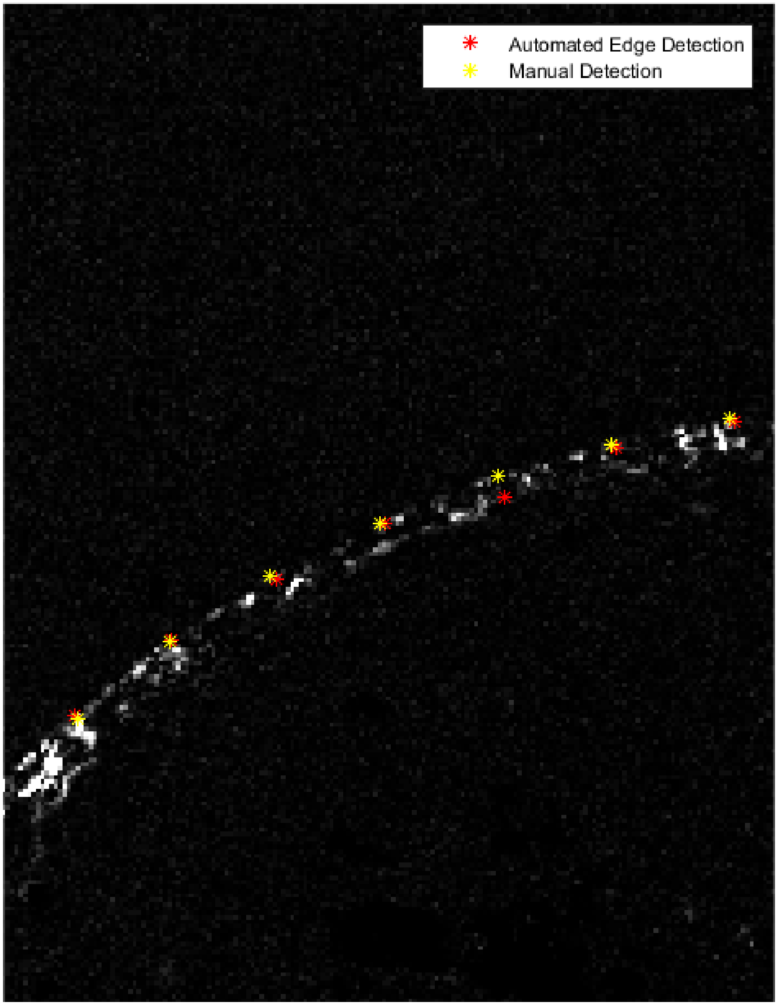

Figure 3.6: This figure shows an enlarged section of a shock wave in a BOS image. The locations found using the careful manual detection and the automated detection are shown.

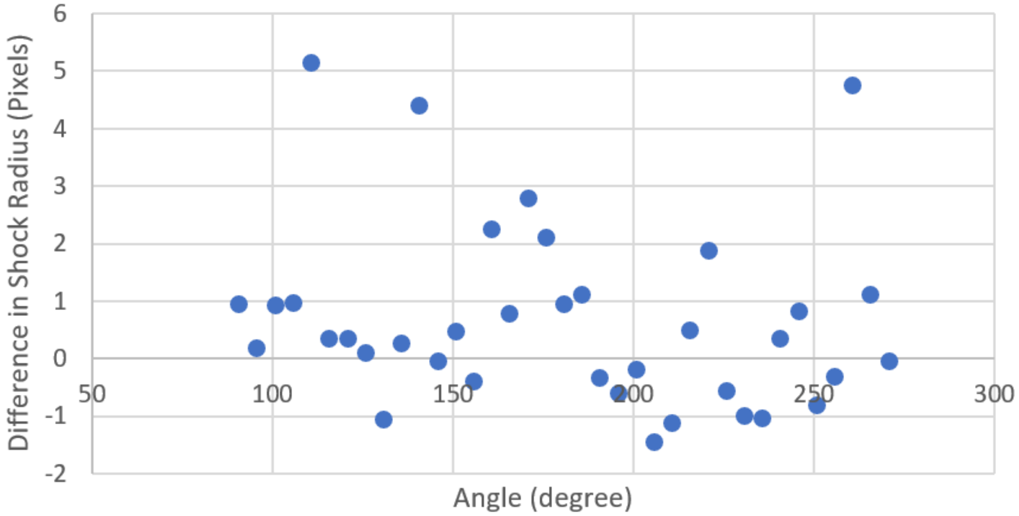

Figure 3.7: Plot of the difference between the careful manual detection points and those found with the automated edge detection method.

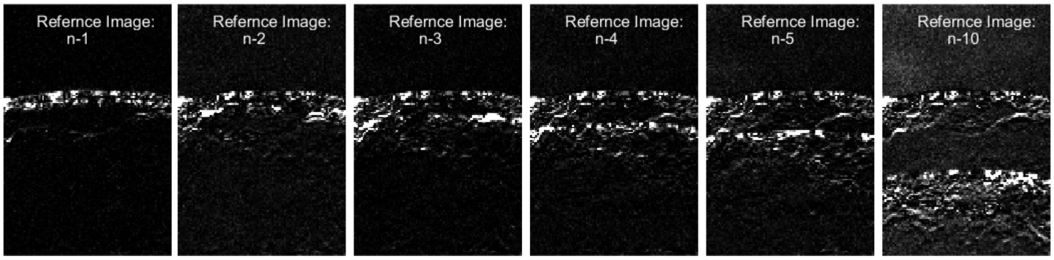

Figure 3.8: BOS images of t=4.5ms from the master camera generated using the reference images noted at the top of each image. The images have been cropped and enlarged to make differences more visible.

The resulting total uncertainty is similar to that of the n-1 image or sequential subtraction. Figure 3.9 shows that of the approaches studied, sequential subtraction is the optimum BOS process to use with the automated detection algorithm, by having a high accuracy while limiting back ground noise.

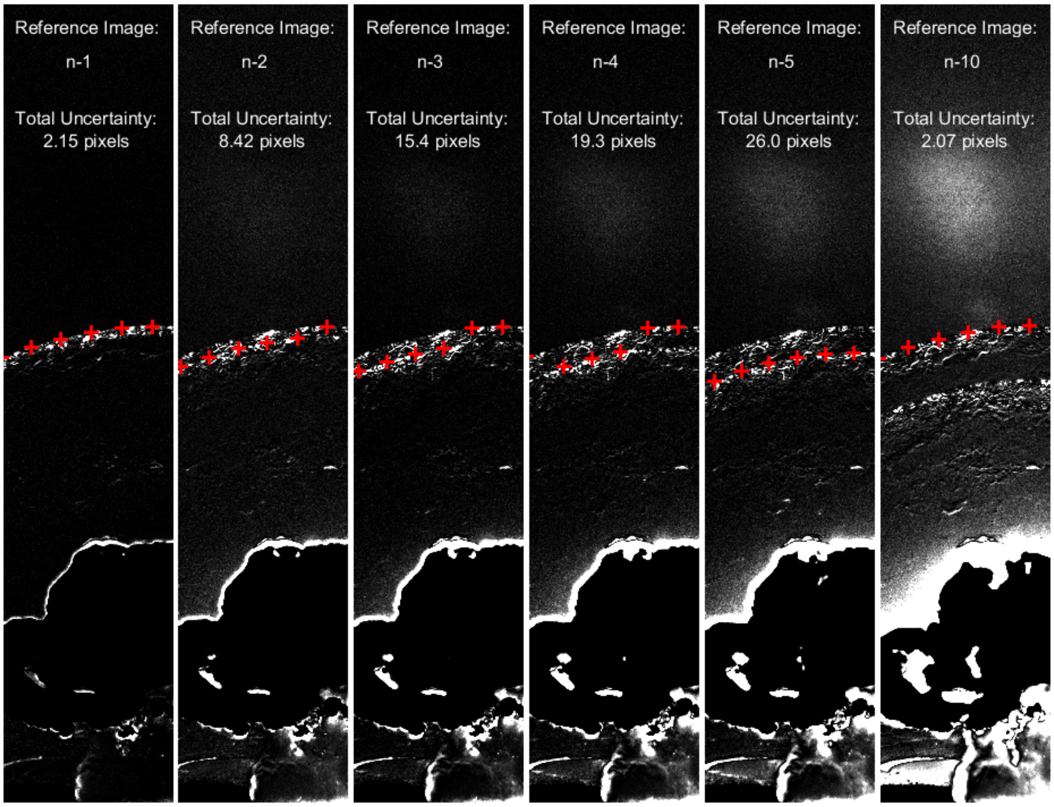

Figure 3.9: BOS images generated using the reference image denoted at the top of each image. The identified shock wave locations are shown in red and the total uncertainty determined for each method is listed.

CHAPTER 4

EXPERIMENTAL RESULTS AND DISCUSSION

4.1 Shock Propagation Measurements

Four high speed cameras imaged the shock wave produced by the detonation of 113 g of C4. The high speed cameras were arranged with a range of angles and at different elevations as described in Section 2.1. The images from each camera were processed into BOS images using the methods described in Section 2.4. The location of the shock wave was then extracted from the BOS images using the automated detection algorithm described in Section 3.3. The radius at each location was then calculated by applying the camera calibration values as described in Section 2.3. The data were then processed to produce a three-dimensional shock wave location as a function of time.

4.1.1 Analysis of Data from Single Test

A spherically-symmetric test was performed to document the ability of the four cameras to accurately measure the same shock propagation. Test 1 in Table 2.1 used a bare charge of 113 g of C4. No fragmentation packet was attached to the charge since the fragments would cause asymmetries in the shock wave.

The result of this test was a set of shock wave radii as a function of time from each camera. Figure 4.1a shows the identified locations of the shock wave from the master camera at time t=3.2 milliseconds, where t=0 is the initiation of the detonator. The radius of these points was determined and scaled using the single camera calibration parameter. These scaled radii are plotted as a function of angle along with a 5% error bar in the Figure 4.1 graph. This total uncertainty was determined by propagating the uncertainties calculated for the single and stereo camera calibrations, which is covered in Section 2.3 and are approximately 2% and 1% respectively, and the uncertainty in the automated detection algorithm, which are covered in Section 3.3, which is between 1-2% over the range of radii examined. All of the radii found for the shock wave were effectively equivalent. This indicates that over the range measured the shock wave is circular, which is expected for a bare charge.

The radius-time graph in Figure 4.1 was expanded by including the scaled radii from the other three cameras and is shown in Figure 4.2. This figure shows

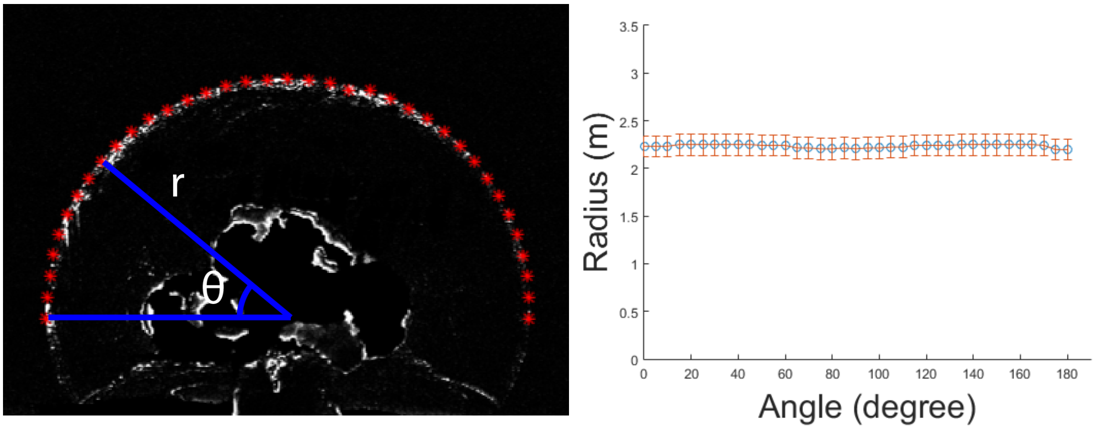

(a)

(b)

Figure 4.1: (a) BOS image taken with master camera of Test 1. The identified locations of the shock wave are shown as red dots. Each location is defined by the radius *r* and the angle θ.(b) The radius of each of the identified locations plotted as a function of angle. A error bar of 5% has been shown over each data point. Note that the angle is defined from the horizontal blue line. As a result points are defined from left to right.

that all of the identified points have an equivalent radii within error. This supports the argument that the shock wave is spherical over the measured area, because each of the rotated cross sections is circular and equivalent. This also indicates that the single camera calibration procedure is functioning properly. If the camera calibration was providing erroneous values then each camera would have points at a different radii. The overlap in radii between cameras supports that the error in camera calibration is within the stated uncertainty.

To examine if the identified shock wave locations remained grouped over time, Figure 4.3a shows each shock wave location plotted at the time it was measured. The locations appear to remain grouped while the mean radius increases with time. This matches the expected behavior of a spherical shock wave expanding radially. Past t=4 ms the shock wave has expanded to the point that it begins to exit the field of view of the cameras. As the shock leaves the field of view of a camera, the number of locations recorded decreases until the shock is no longer recorded by a given camera. To quantify the spread of the locations as a function of time, the mean and standard deviation at each time were calculated and are shown in Figure 4.3b. As expected, the mean radius increases smoothly over time with no jumps or sudden changes in slope. Conversely the standard deviation fluctuates with time. This indicates that the spread in the data is due to the precision of the measurement and not the shock wave becoming more or less asymmetric with time.

To further study the precision with which the radii were measured, the statistical frequency of the standard deviation is plotted in Figure 4.4, with the

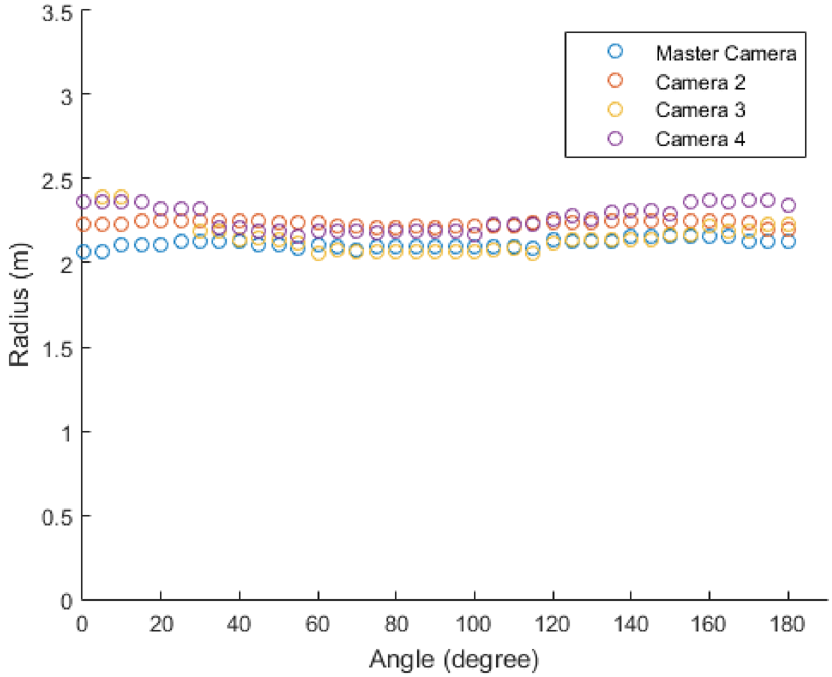

Figure 4.2: Plot of the radius of each identified point as a function of angle aggregated from all cameras for test 1 at t=3.2 ms.

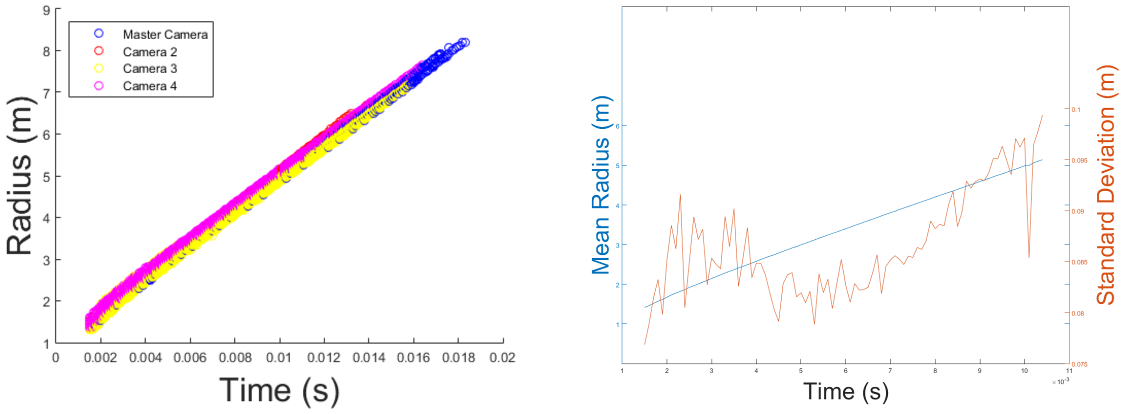

(a)

(b)

Figure 4.3: Shock wave radius as a function of time data from Test 1 showing (a) all data points from all cameras and (b) the average radius versus time and the associate standard deviation in the radius at each time.

bin size determined by Scott's rule [43]. This figure shows the standard deviation of radii in Test 1 is distributed around 84 mm. This value is similar to the previously stated 5% uncertainty applied to the early range of radii measured, indicating the precision of the measurement is within the 5% is uncertainty value. The maximum, minimum, and mean standard deviation are listed in Table 4.1.

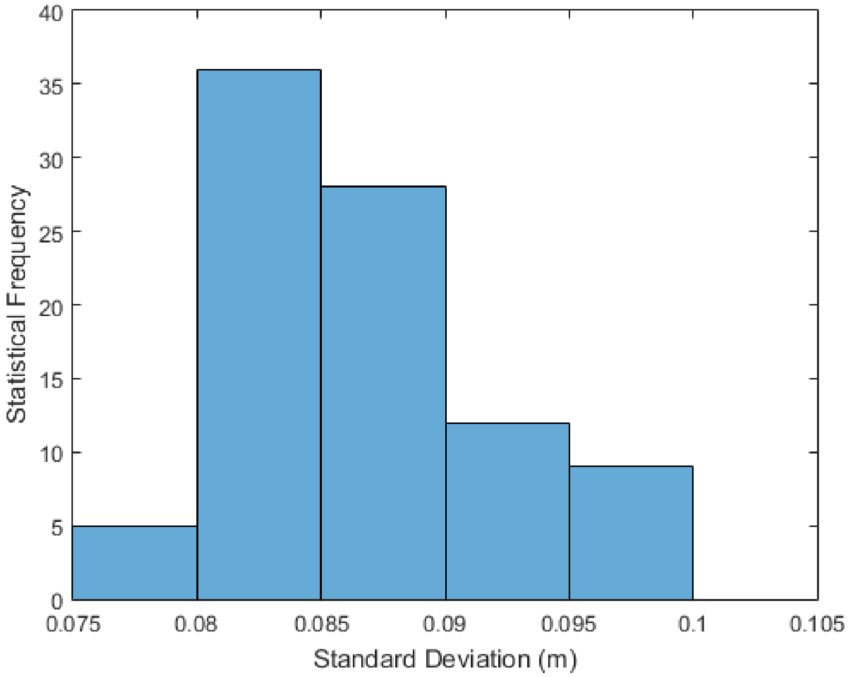

Figure 4.4: The distribution of standard deviations of the radii at each time binned using Scott's rule.

Since the shock wave has been shown to be spherical it can be reasonably described as a one-dimensional function of time and radius. To that end, the cumulative radius time measurements were fit to the Dewey equation, Equation 1.6. The resulting fit and fitting parameters are shown in Figure 4.5 and listed in Table 4.2. These parameters can be used to describe the shock wave's position and velocity within the area measured. Because the Dewey fit is taken over so many points the uncertainty stemming from the automated point detection algorithm is effectively reduced but the error originating in the single camera calibration is unaffected. The uncertainty in these values is thus taken as equivalent to the uncertainty in the single camera calibration, which is approximately 2%. As the shock wave expands, the number of shock locations recorded at each time decreases. The low number of recorded locations biased the fitting parameters resulting in non-realistic results. To remove this bias effect, only the times where a majority of the shock wave was visualized by each camera were fitted to the Dewey equation. To determine the exact cut off time, the angle over which the shock wave was visualized in each frame was compared to the angle from the first measured frame. The time at which the ratio dropped to 0.5 or below was used as the cut off. This time is denoted in Figure 4.5 as the vertical black line.

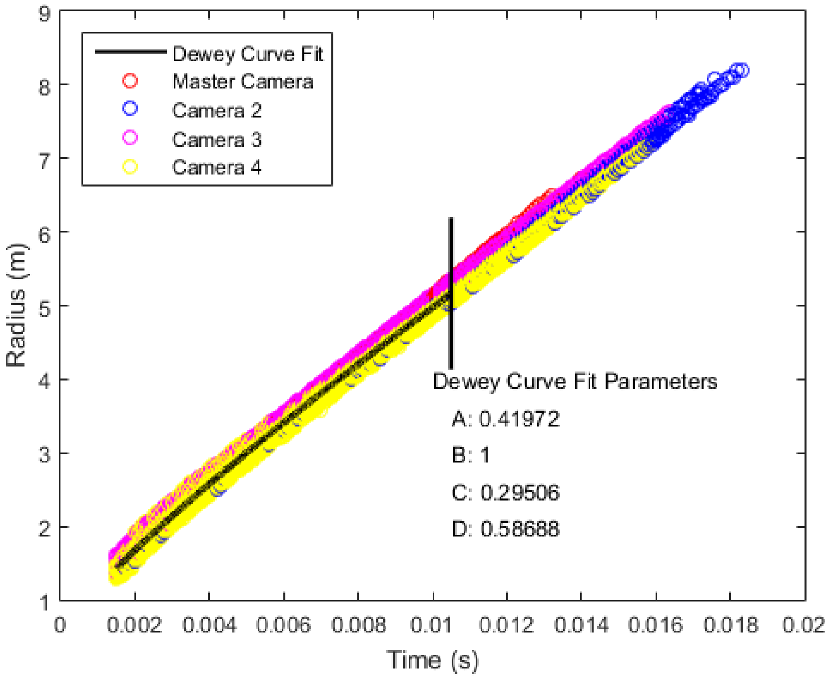

Figure 4.5: The Dewey curve fit is shown over a plot of the radius of each identified point as a function of time from each camera for Test 1. The black vertical line indicates the time below which was fit to the Dewey equation. The Dewey curve fitting parameters are also shown.

4.1.2 Fitting Data to Three Dimensional Surface

The shock wave location data were fit to a three dimensional surface that describes the shock wave. Figure 4.6 a-d show the identified locations in each camera view at time t=5 ms. These two-dimensional locations were then rotated with the respective rotation matrix to match the camera rotation found using the stereo camera calibration. The shock wave locations from each rotated camera view are then merged into a single point cloud for each time. Figure 4.6e shows a point cloud from Test 1 with the points from each camera labeled. The figure shows how each camera defines a single plane of the shock wave. The entire point cloud was then processed by a sphere fitting algorithm into a spherical surface [41], which is shown in Figure 4.6f. This geodesic sphere is centered at the origin, which is the pre-test location of the explosive, and generated from the radius found using the sphere fitting algorithm.

When the radii determined by the sphere fitting algorithm is compared to the radii determined by the Dewey curve fit there was found to be a difference ranging from 0.7% to 3.4%, with the a mean difference of 1.0%. The discrepancy between the two methods is attributed to the different data sets they are fitting. The sphere fitting algorithm determined the best radius for each time whereas the Dewey curve fit is fitting a single continuous curve to the radius across all times. Since the Dewey method is fitting across a wider range it minimizes the effect of individual measurements producing a more consistent radius. In this limited case, of a spherical shock wave, the Dewey curve fit is the better method to determine the radius but is not a valid method for reproducing elliptical or asymmetric shock waves. In these cases the points from an individual frame would need to be fit to a surface of a given shape.

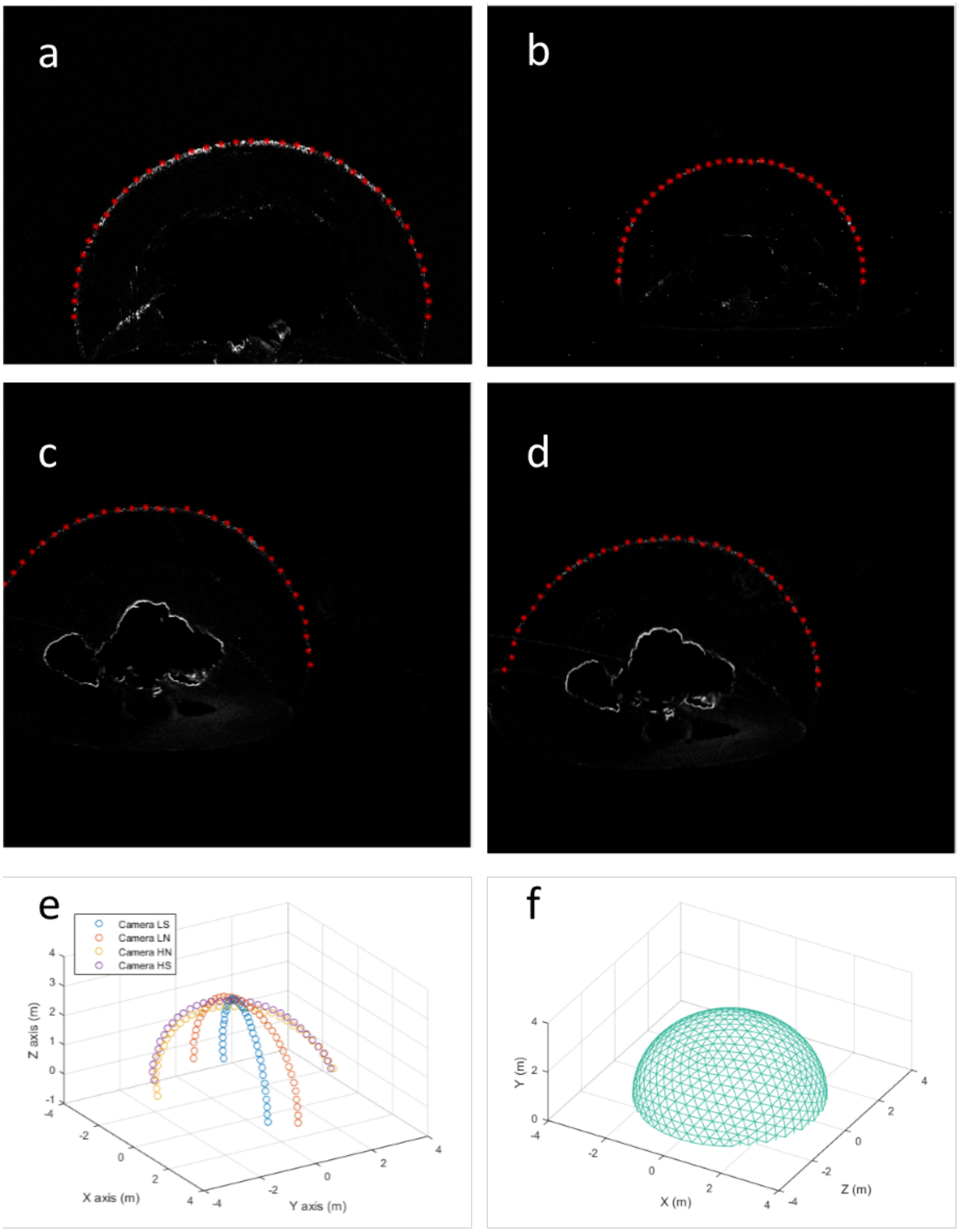

Figure 4.6: (a-d) BOS images of Test 1 at t=5 ms taken from cameras Master, 2, 3 and 4, respectively. The identified points are shown plotted on each BOS image. (e) The point cloud generated by rotating each of the above found points with the rotation matrix determined with the stereo camera calibration. (f) The surface found by applying the sphere fitting algorithm to the point cloud.

4.1.3 Analysis of Data from Multiple Tests

The procedure outlined in section 4.1.1 was used to analyze the remaining tests outlined in Table 2.1. Figure 4.7 a-d shows the BOS image from the master camera 3.2 ms after detonation for each test. The identified shock locations from each image are plotted as a function of angle in Figure 4.7 e-h. Test 2 contained steel fragments, and the bow shock from these fragments distorted the primary shock from the explosive, causing it to elongate. This effect can be seen in Figure 4.7b as the shock wave stretching to the left. This distortion can be seen in Figure 4.7f as the upwards trend in radius as the angle increases past 100 degrees.

Test 3 used the same type of steel fragments as Test 2 but did not experience the same level of shock wave distortion. Figure 4.7c shows the shock is slightly distorted on its left side. This distortion made it difficult to visualize the shock wave and to measure the shock location. As such it appears that the shock wave is not distorted much. Figure 4.7g shows that the area of the shock that was well visualized was radially symmetric, but note that the measurements are over a more limited region and it is not expected that the entire shock is symmetric.

Test 4 contained acrylic fragments, which caused very large distortions in the visible shock wave. Figure 4.7d shows how the shock was formed into a large ellipse which results in the upward-facing curve of the radius angle data in Figure 4.7h.

Despite the fact that each of these test used the same type and amount of explosive, each test produced very different shock waves as a result of including the fragmentation devices. Significant variation was even observed in the two Tests (2 and 3) that used the same fragmentation device. This figure shows the ability of the presently-developed reconstruction techniques to detect and measure asymmetries in shock waves. It also demonstrates why the assumption of a symmetric shock wave is not valid in many explosive tests.

One measure of the asymmetry of a shock wave is the standard deviation of its radii, with larger standard deviations indicating greater asymmetries. The standard deviation at each time for the tests was calculated and the statistical properties listed in Table 4.1. The two tests that were radially symmetric over the area measured, Test 1 and 3, have radii that are spread over a narrow band, which can be seen in Figure 4.7e and g. As a result they have low mean standard deviations of 84 and 101 mm, respectively. Tests 2 and 4 had asymmetric shock waves, which caused their radii to be spread out over a larger band, which is shown in Figure 4.7f and h. Test 4 had the most asymmetric shock, which can be determined by noting it has the highest standard deviation of 222 mm. In examining Figure 4.7, Test 2 appears to actually have the most asymmetric shock wave, but the shock wave is not being detected over the entire field of view. The shock wave in Test 4 is more clearly identified throughout the imaging area, with identified points across the entire shock front. The statistics are based on all of the identified shock wave points, so Test 4 results in a larger standard deviation even though the images show differently. The standard deviation and symmetry

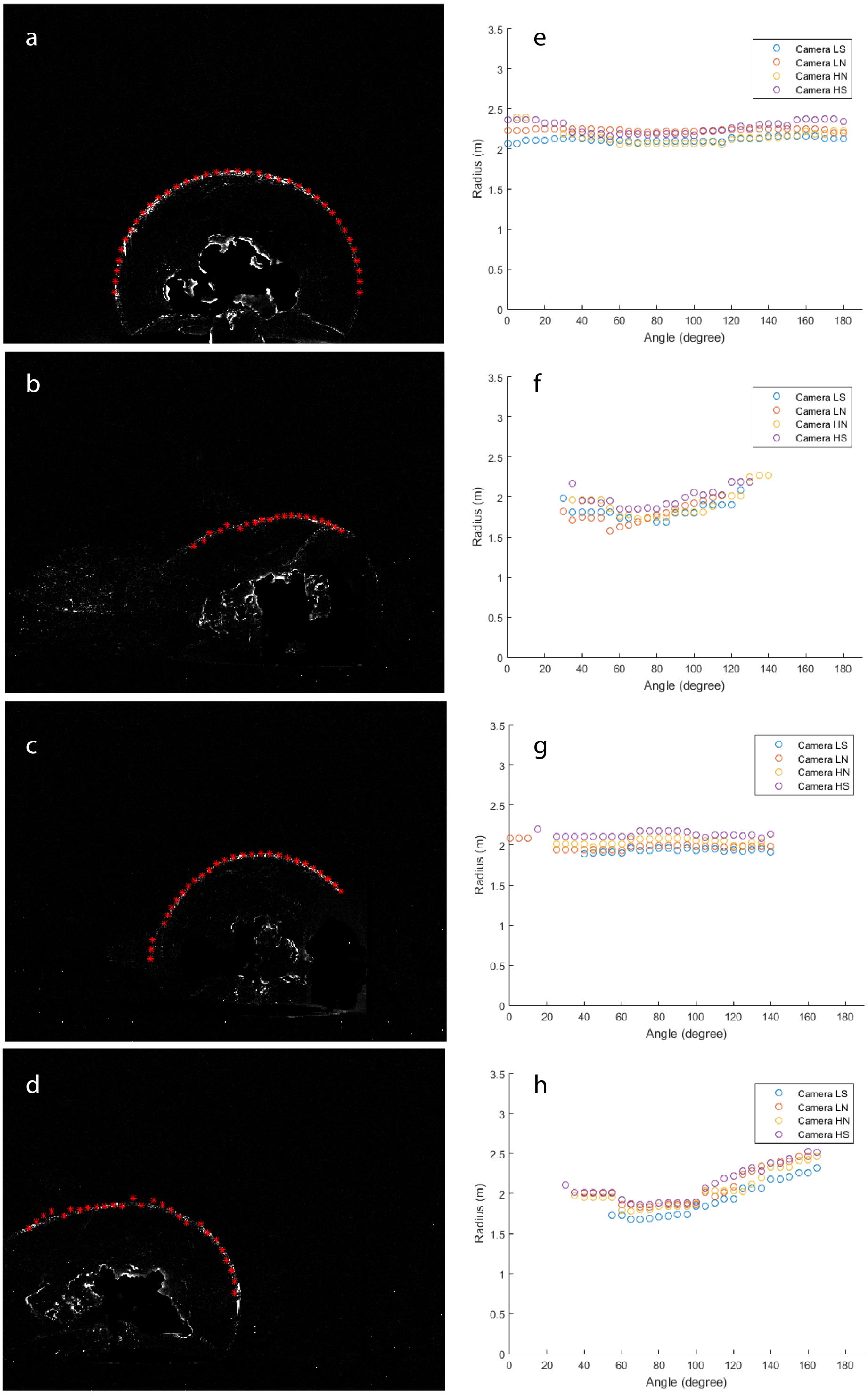

Figure 4.7: This compares all tests at t=3.2 ms. (a-d) are the BOS images taken by the master camera for Tests 1-4, respectively. The identified points are shown on each shock wave as red dots. (e-h) is the plots of the radius of each point as a function of the point's angle for each respective test.

Table 4.1: List of statistical characteristics of the standard deviations of radii for each time from each test.

Test Number	Mean σ (m)	Maximum σ (m)	Minimum σ (m)
1	0.0866	0.0994	0.0769
2	0.1636	0.2055	0.1196
3	0.1015	0.1449	0.0637
4	0.2220	.2572	0.1778

Table 4.2: List of parameters for the Dewey curve fit equation from each test.

Test Number	A:	B:	C:	D:	Angle Range (θ)	Time Range Fitted (ms)
1	0.41972	1	0.29506	0.58688	0-180	15-105
3	0.12833	1	-0.17987	1.1412	20-180	15-74
4	0.51805	1	0.37013	0.45054	135-180	15-95

measurements commented on here are limited to the regions of the shock wave that are automatically detected.

Test 1 produced a radially symmetric shock wave so it was valid to describe it using the Dewey curve fit. Test 3 did not produce a symmetric shock but the distorted, asymmetric parts were not well visualized. The area that was visualized was determined to be symmetric so the data were fit using the Dewey curve fit. The time radius data as well as the Dewey curve fit and parameters are shown in Figure 4.8 and the parameters listed in Table 4.2. Fitting a portion of shock is a valid technique so long as the resulting parameters are only used to describe the portion of the the shock wave that was originally measured.

Test 4 produced an asymmetric shock wave so fitting the entire shock to the Dewey equation would not be appropriate. To compare the optical data to pressure probe data the portion of the shock that passed over the pressure probe was isolated. The section of the shock wave between 135 and 180 degrees was isolated and fit to the Dewey equation. The section of the shock that was isolated and the resulting Dewey curve is shown in Figure 4.9 and the fitting parameters are listed in Table 4.2. Since this section is not symmetric it has a higher uncertainty of 2.5%. The ability to characterize isolated sections of an asymmetric shock is useful because most explosive articles do not produce perfectly spherical shock waves. This allows the shock wave effects, which can be predicted by the Mach-radius curve, to be established as a function of radius and angle for a specific explosive article. To this end, the fitting parameters were used in Equation 1.7 to plot the Mach-radius curve, which is shown in Figure 4.10.

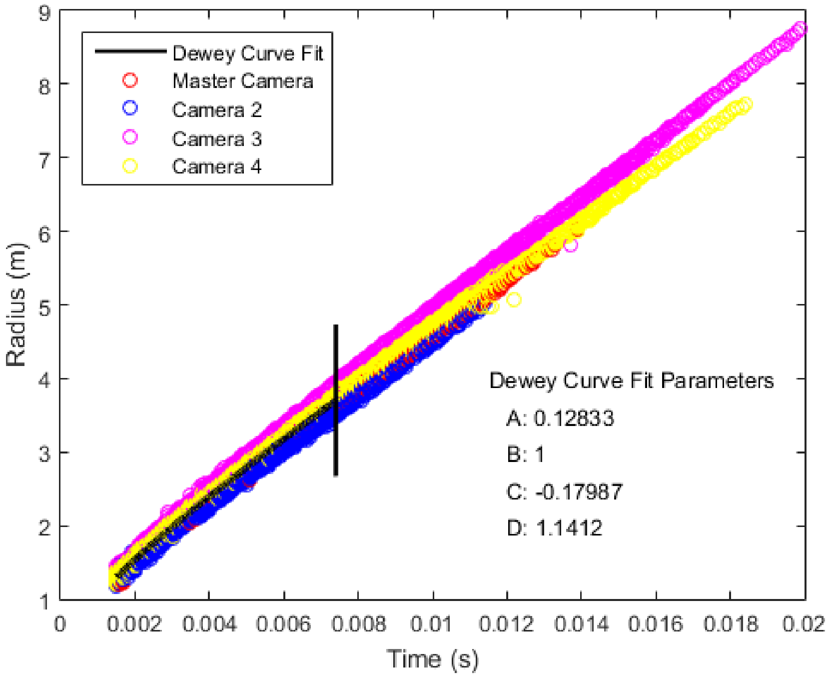

Figure 4.8: The Dewey curve fit is shown over a plot of the radius of each identified point as a function of time from each camera for Test 3. The black vertical line indicates the time below which was fit to the Dewey equation. The Dewey curve fitting parameters are also shown.

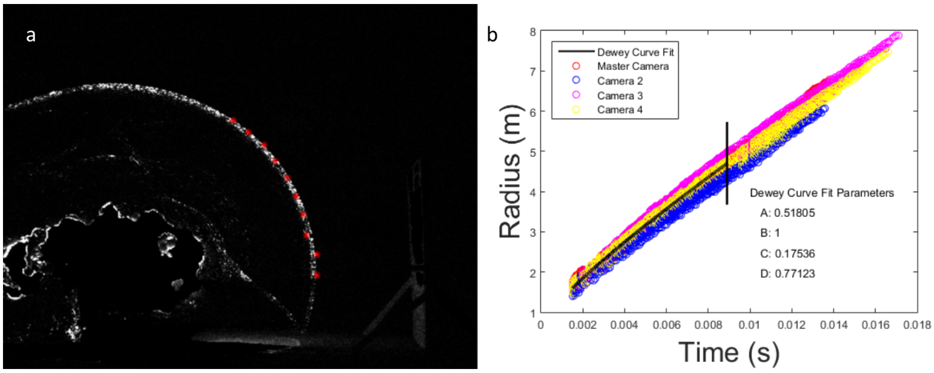

Figure 4.9: (a) A BOS image of Test 4 taken by the master camera. A 45 degree potion of the shock has been isolated and the identified points in this section are shown. (b) The points of the isolated section where plotted as a function of time and fit to the Dewey equation. The black vertical line indicates the time below which was fit to the Dewey equation.

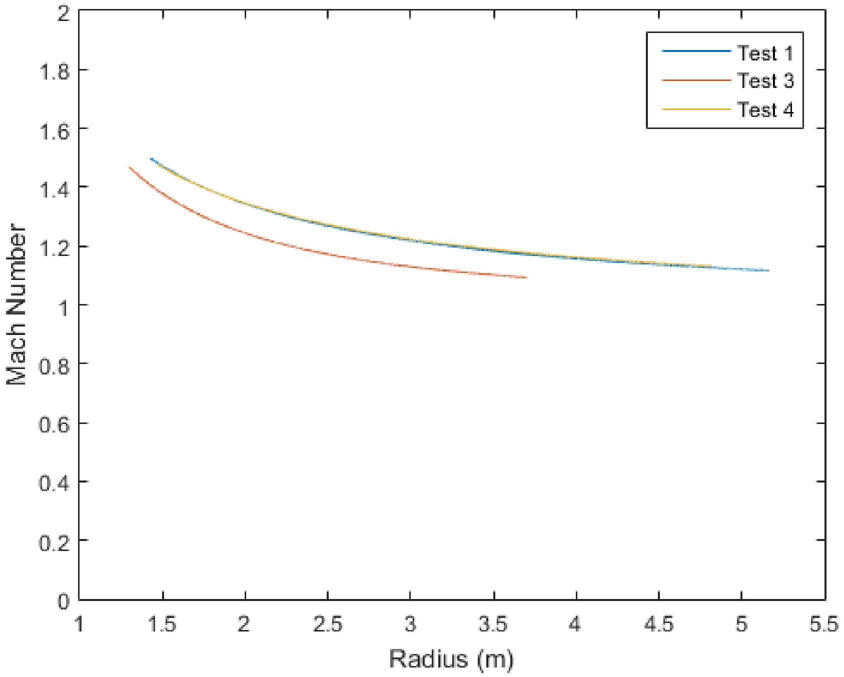

Figure 4.10: The Mach-radius curve for the sections of Test 1, 3 and 4 over the time period they were fitted to the Dewey equation.

4.2 Comparison of Optical and Pressure Data

In addition to optical data, pressure traces were recorded during Tests 2, 3 and 4. The pressure transducer was used to identify time of arrival and peak overpressure behind the shock wave, as well as recording the pressure decay and overall impulse. The optical shock tracking data is used to calculate time of arrival from the images and peak overpressure from the shock Mach number using Equation 1.8.

When a shock wave reaches a pressure transducer it is recorded as a sharp jump in the pressure trace. This discontinuity can be easily detected and reported as the time of arrival of the shock wave. The uncertainty in this time is related to the sample rate of the oscilloscope and the sensitivity of the probe. In Test 4, the time of arrival of the shock wave at the pressure probe, which was at a distance of 4.5 m from the center of the explosive charge, was determined to be 8.96 ± 0.01 ms from the pressure gage record.

There are two methods to determine the time of arrival using refractive imaging. The simplest method is to review the BOS images and record the frame number, and corresponding time, where the shock wave passes over the point of interest. This method can be complicated if the point of interest is not in the same plane as the plane the shock wave is visualized in. A way to avoid this three-dimensional effect is to have a reference point that is in the plane the shock is visualized that is equidistant with the point of interest. In Figure 4.11a the pressure transducer was placed equidistant to the charge as the reflection wall. This setup allows for the assumption that the shock will reach the pressure probe and reflection wall simultaneously. The minimum time uncertainty in this method is equal to the inverse of the frame rate of the camera and increases in uncertainty with growing uncertainty with which the points are located equidistant. From Figure 4.11a the time of arrival of the shock wave can be determined to be 8.9 ± 0.1 ms.

A second method to determine time of arrival is to use the radius-time curve for the shock wave. If the distance between the charge and point of interest is known, then the radius is selected on the curve and the corresponding time noted. If the exact distance between the charge and point of interest is known and there is high confidence in the Dewey curve fit this method works well. Because Test 4 had a uncertainty in the Dewey curve fit of ±2.5%, and the distance between the charge and pressure probe was only measured to an accuracy of ±0.1 m this method had a high uncertainty. Using the radius-time curve method the time of arrival was determined to be 8.6 ± 0.4 ms.

If there is only a single point of interest and the camera can be placed so that it will visualize the shock moving over the point, then the optical pass over method can be implemented easily and accurately. If there are multiple points of interest in a variety of planes and each point's location is well known then the using radius-time curve is the optimum method. Regardless of how well these two optical techniques are implemented they will not reach the precision of pressure transducer time of arrival, simply because the transducer is able to sample at much higher rates than a commercial high speed camera which is imaging a large field of view.

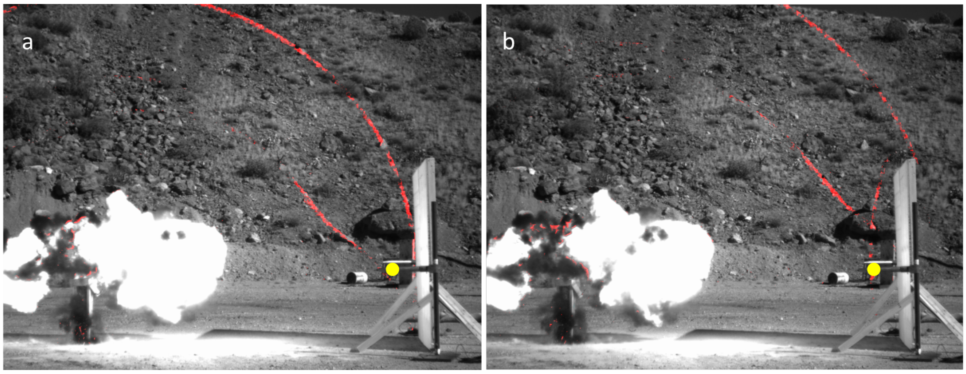

Figure 4.11: BOS images over-laid in red on the direct image to show the shock wave location at (a) t=8.9 ms and (b) t=10 ms. The location of the pressure transducer is displayed as a the yellow dot.

The peak over-pressure value is often taken as the highest value in the pressure trace. Due to the limited response time of pressure transducer this value is often greater than true peak pressure [38]. This results in a larger uncertainty in the peak pressure value than the error reported by the manufacturer for a given pressure transducer. Figure 4.12 shows the pressure trace from Test 4. The peak pressure shown in this pressure trace was 3.5 ± 0.25 psi.

Peak pressure can also be determined by analysis of the optical data. Equation 1.8 relates peak pressure to the Mach number of a shock wave. The Mach number at a given location can be determined from Figure 4.10. Using the time of arrival data from the optical pass-over method the exact distance between the charge and pressure probe was determined. This distance was then used to determine Mach number and the resulting peak over-pressure of 3.3 ± 0.9 psi. The optically-measured peak pressure is plotted on Figure 4.12 at the time of arrival found using the optical pass over method. The error bar for time is smaller than the size of the point with the error bars for pressure shown. The error in pressure was determined by propagating a 2.5% uncertainty in Mach number. When the shock wave reached the pressure probe the Mach number had decayed to 1.11 ± 0.03. Because the Mach number is close to unity, small variations in value cause larger percent variations in pressure, resulting in the larger uncertainty in pressure.

The optical data is also able to make pressure trace data more useful. Figure 4.12 shows two large pressure spikes, the first corresponds to the time of arrival of the shock wave. From examining the pressure trace the origin of the second spike cannot be established. Figure 4.11b shows the BOS image overlaid on the direct image at that time. This image shows that the reflected ground shock is the source of the second pressure spike. The visualized ground reflection reaches the reflecting wall at the time of the second spike. The reflection from the

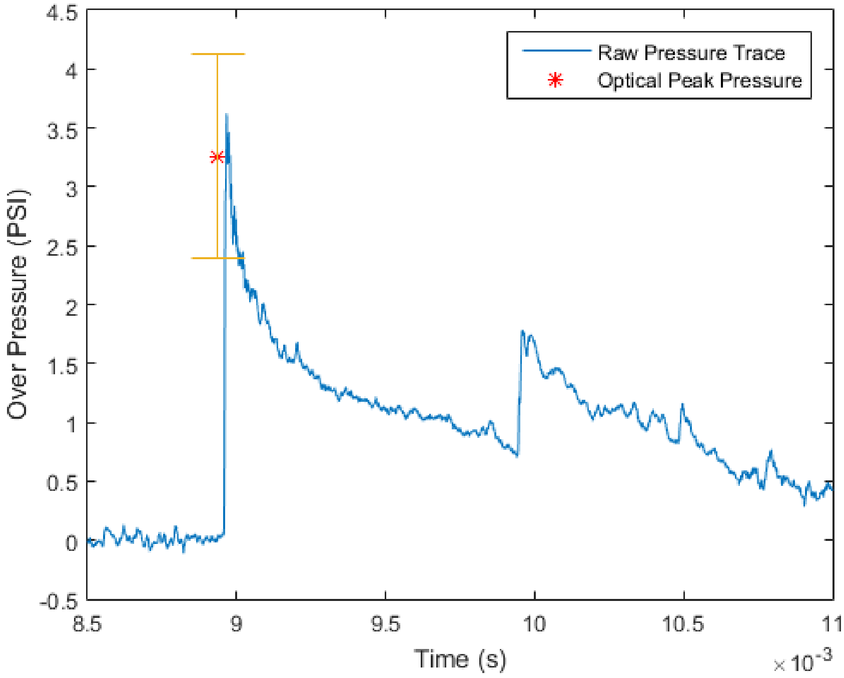

Figure 4.12: The pressure trace of Test 4 with the optically determined peak overpressure shown.

wall is visualized over the pressure probe at the same time but due to the three dimensional effects this shock has not yet reached the probe.

CHAPTER 5

CONCLUSION AND FUTURE WORK

5.1 Summary and Conclusions

The proliferation of modern high speed digital cameras has made large scale background oriented schlieren (BOS) imaging practical for modern explosive testing. This technique uses commercial high speed cameras and the existing landscape to generate refractive images of the shock wave and product gases generated by explosives as well as capturing any explosively driven fragments. BOS systems can be calibrated allowing for the size and shape of the shock wave to be measured. As the shock wave expands through the field of view, any reflections or distortions caused by objects in the test arena can be tracked. These capabilities make large scale BOS imaging capable of recording critical aspects of explosive tests.

The location of shock waves and other refractive features in BOS images are often located by hand. Although accurate, this method is slow and requires training. By understanding the compressible flow that underlies these phenomenon an automated shock wave detection developed algorithm was developed to track shock waves in BOS images. The algorithm was able to determine the location of a shock front with a similar accuracy to manual detection but at much greater speeds. This MATLAB script can be easily incorporated into existing or future algorithms that process BOS images.

By recording explosive events with multiple BOS systems the three-dimensional shape and size of the shock wave can be measured. The intrinsic and extrinsic camera characteristics can be determined by well-established camera calibration techniques. These camera characteristics were used to combine the individual shock wave cross sections recorded by each BOS system into a single point cloud. A surface was fit to the three-dimensional point cloud to describe the shock wave surface. This surface was used to track and visualize the shock wave growth as a function of time.

Using refractive imaging, automated point detection, and camera calibration techniques the shock wave from four unique tests were characterized. Multiple points on the shock waves were identified and their radii calculated. These radii were compared as a function of angle and time to evaluate how symmetric each shock wave was. It was found that shock waves ranged from symmetric to highly asymmetric. The identified shock wave locations were also combined into point clouds and fit to spheres describing the shock wave surfaces. The sphere fitting algorithm was found to have a higher uncertainty than the Dewey fit but developing an approach to fitting a surface to the entire point cloud will be necessary when examining asymmetric cases. Where applicable, the shock wave radii were fit to the Dewey equation so that blast effects, such as overpressure, could be determined. The overpressure estimation was found to have high uncertainty resulting from uncertainty in the Dewey fit and because the Mach number was approaching unity. The time of arrival was determined optically using two methods and compared with time of arrival determined by a pressure transducer. The optical methods produced a similar time of arrival to the pressure transducer but lacked the pressure transducers' precision. In total, optical methods were shown to be capable of characterizing explosively driven shock waves.

Overall, the presented research has demonstrated the utility of multi-camera background oriented schlieren imaging in explosive testing. BOS imaging can be implemented using commercial cameras in many experimental setups with no modifications. The BOS images can then be processed quickly and accurately into a three-dimensional representation of the shock wave. The optical data can be used independently or paired with traditional analysis techniques to better understand the shock wave produced by an explosive event.

5.2 Future Work

The current MATLAB script used for automated shock wave detection only functions for BOS images. Shock waves visualized with shadowgraph or schlieren are similar to those visualized with BOS. With minor adjustments the automated detection algorithm could be used to detect shock waves in the three main refractive imaging techniques: schlieren, shadowgraph and BOS.

The sphere fitting algorithm used to generate the geodesic sphere is incapable of recreating non-spherical shocks. By replacing the sphere fitting algorithm with a more robust algorithm a surface could be fit to the points without pre-defining the end shape. This would allow for the recreation of more complex shock waves and asymmetries with in shock waves.

The current work focused on using multi-camera background oriented schlieren imaging on shock waves with limited complexity. This technique will be most useful in examining shock waves in highly complex and dynamic systems. This technique could be used to study how shock waves reflect and interact in complex closed systems such as inside of a building with multiple rooms and halls. It could also be used to study dynamic shock reflections such as Mach reflections.

APPENDIX A

AUTOMATED DETECTION MATLAB CODE

```
%variables defined earlier in script
% center: This is a [2,c] matrix where c is the number of cameras used.
%This matrix holds the location of the charge as recorded in each camera
%view,
% AngleCenter: This is a vector which holds the angles which will be
%searched for the shock wave
% Sections: This is the length of the vector "AngleCenter"
% SeedDist: This is an estimate of where the shock wave is located
% SeedGrowth: This is an estimate of how many pixels the shock wave will
% grow between frames.
% Boxlength: This variable adjusts how large of an area is search for
% the shock wave


%this section will do the autodetect
%_________________________________________________________________
%find search parameters

%generate search location
%___________________________________________________________________________
%this will find center of boxes

for a=1:Sections;
    x(a)=center(1,c)+cos(deg2rad(AngleCenter(a)))*SeedDist(c);
    y(a)=center(2,c)-sin(deg2rad(AngleCenter(a)))*SeedDist(c);
end

%This will set up for the next loop
SeedDist(c)=SeedDist(c)+SeedGrowth(c);

%this will find the bounding box
for a=1:Sections;
    BoxBR(a,:)=[round(x(a)+BoxLength),round(y(a)+BoxLength)];
    BoxTL(a,:)=[round(x(a)-BoxLength),round(y(a)-BoxLength)];
end
%___________________________________________________________________________

[n,m]=size(image);
```

```
MaxSearchOptions(3)=m;
MaxSearchOptions(2)=sqrt(center(1,c)^2+center(2,c)^2);
MaxSearchOptions(1)=sqrt(center(1,c)^2+(center(2,c)^2));

SearchMax=max(MaxSearchOptions);

%Autdo detect sequence
clear bins %this should eliminate rewrite errors
clear holder
clear MaxDist
clear BombCentered
%Autdo detect sequence
for Szone=1:Sections; %this will select which box to search in
    holder=zeros(SearchMax,1);
    for xsearch=BoxTL(Szone,1):BoxBR(Szone,1);
        for ysearch=BoxTL(Szone,2):BoxBR(Szone,2);
            d=round(sqrt((xsearch-center(1,c))^2+(ysearch-center(2,c))^2));
            if 0<xsearch & xsearch<m & 0<ysearch & ysearch<n;
                holder(d)=holder(d)+double(image(ysearch,xsearch));
            end
        end
    end
    DifBins(:,Szone)=diff(holder(:));
end



%calculate the shock distnaces and then corrisponding x y possitions
for i=1:Sections
    if 400<max(bins(:,i));%EXPERIMENTAL this section will remove data
%points of low signal to noise ratio
        MaxDist(i)=min(find(DifBins(:,i)==min(DifBins(:,i))));
    else
        MaxDist(i)=0;
    end
    BombCentered(i,:)=[cos(deg2rad(AngleCenter(i)))*MaxDist(i),sin(deg2rad-
-(AngleCenter(i)))*MaxDist(i)];
end

%this section will plot points on initial imagee

if powerswitch(4);
    figure('name',CurrentImage),imshow(image);
    hold on
    plot(center(2,c),center(1,c));

    for i=1:Sections;
        hold on
        plot(BombCentered(i,1)+center(1,c),center(2,c)-BombCentered(i,2)-
-,'R*');
    end
```

```
    if powerswitch(7);
        if framenumber>(FirstFrame+10);
            DeleteImage=[test ' ' cam ' ' num2str(framenumber-10)];
            close (DeleteImage);
        end
    end
end

%END AUTODETECT
%_______________________________________________________________
```

REFERENCES

[1] G.S. Settles. *Schlieren and Shadowgraph Techniques: Visualizing Phenomena in Transparent Media*. Experimental Fluid Mechanics. Springer-Verlag Berlin Heidelberg, 1 edition, 2001.

[2] M. J. Hargather and G. S. Settles. A comparison of three quantitative schlieren techniques. *Optics and Lasers in Engineering*, 50:8–17, 2012.

[3] G. S Settles and M. J Hargather. A review of recent developments in schlieren and shadowgraph techniques. *Measurement Science and Technology*, 28, 2017.

[4] H. E. Edgerton. Shockwave photography of large subjects in daylight. *Review of Scientific Instruments*, 29(2):171–172, 1958.

[5] M. J. Hargather and G. S. Settles. Retroreflective shadowgraph technique for large-scale visualization. *Applied Optics*, 48:4449–4457, 2009.

[6] P. M. Giannuzzi, M. J. Hargather, and G. C. Doig. Explosive-driven shock wave and vortex ring interaction with a propane flame. *Shock Waves*, 26:851–857, 2016.

[7] M. J. Hargather, G. S. Settles, and J. A. Gatto. Full-scale optical experiments on the explosive failure of a uld-3 air cargo container. In *4th International Aviation Security Technology Symposium*, Washington, D.C., November-December 2006.

[8] M. Raffel. Background-oriented schlieren (bos) techniques. *Experiments in Fluids*, 56:60:1–17, 2015.

[9] H. Schardin. Die schlierenverfahren und ihre anwendungen. *Ergebnisse der Exakten Naturwissenschaften*, 20:303–439, 1942. Translated as NASA TT F-12731.

[10] S. B. Dalziel, G. O. Hughes, and B. R. Sutherland. Synthetic schlieren. In G. M. Carlomagno, editor, *Proc. 8th International Symposium on Flow Visualization*, volume 62, Sorrento, Italy, 1998.

[11] G. E. A. Meier. Hintergrund-schlierenverfahren. Deutsche Patentanmeldung, 1999. DE 199 42 856 A1.

[12] M. Raffel, H. Richard, and G. Meier. On the applicability of background oriented optical tomography for large scale aerodynamic investigations. *Experiments in Fluids*, 28:477–481, 2000.

[13] K. Kindler, E. Goldhahn, F. Leopold, and M. Raffel. Recent developments in background oriented schlieren methods for rotor blade tip vortex measurements. *Experiments in Fluids*, 43(2-3):233 – 240, 2007.

[14] M. J. Hargather and G. S. Settles. Natural-background-oriented schlieren. *Experiments In Fluids*, 48(1):59–68, 2010.

[15] M. J. Hargather. Background-oriented schlieren diagnostics for large-scale explosive testing. *Shock Waves*, 23:529–536, 2013.

[16] F. A. Mier and M. J. Hargather. Color gradient backgroundoriented schlieren imaging. *Experiments In Fluids*, 57(95), 2016.

[17] S.B. Dalziel, G.O. Hughes, and B.R. Sutherland. Whole-field density measurements by 'synthetic schlieren'. *Experiments in Fluids*, 28(4):322 – 335, 2000.

[18] G. E. A. Meier. Computerized background-oriented schlieren. *Experiments In Fluids*, 33(1):181–187, 2002.

[19] O. K. Sommersel, D. Bjerketvedt, S. O. Christensen, O. Krest, and K. Vaagsaether. Application of background oriented schlieren for quantitative measurements of shock waves from explosions. *Shock Waves*, 18(4):291 – 7, 2008.

[20] T. Mizukaki, H. Tsukada, K. Wakabayashi, T. Matsumaura, and Y. Nakayama. Quantitative visualization of open-air explosions by using background-oriented schlieren with natural background. In *28th International Symposium on Shock Waves*, Manchester, United Kingdom, 2011.

[21] B. May. *A Village Lost and Found: An annotated tour of the 1850s series of stereo photographs "Scenes in Our Village" by T. R. Williams*. London Stereoscopic Company, 2009.

[22] T. Dunn. 3D spies of WWII. NOVA a BBC/WGBH Co-Production, 2011.

[23] D. Marr and T. Poggio. Cooperative computation of stereo disparity. *Science*, 194(4262):283–287, 1976.

[24] G. Slabaugh, B. Culbertson, T. Malzbender, and R. Schafer. A survey of methods for volumetric scene reconstruction from photographs. In *2001 Eurographics conference on Volume Graphics*, New York, USA, June 21-22 2001.

[25] MathWorks. *MATLAB: Computer Vision System Toolbox*, r2015a edition, 2015.

[26] J. Heikkila and O. Silven. A four-step camera calibration procedure with implicit image correction. In *IEEE Computer Society Conference on Computer Vision and Pattern Recognition*, pages 1106–1116, San Juan, CA, June 1997.

[27] M. Brown and D. G. Lowe. Unsupervised 3d object recognition and reconstruction in unordered dataset. In *3-D Digital Imaging and Modelin,g 2005*. Fifth International Conference on. IEEE, 2005.

[28] F. Klinge, T. Kirmse, and J. Kompenhans. Application of quantitative background oriented schlieren (bos): Investigation of a wing tip vortex in a transonic wind tunnel. In *The 4th Pacific Symposium on Flow Visualization and Image Processing*, volume F4097, Chamonix, France, June 2-3 2003.

[29] B. Atcheson, I. Ihrke, W. Heidrich, A. Tevs, D. Bradley, M. Magnor, and H. P. Seidel. Time-resolved 3d capture of non-stationary gas flows. *ACM Transactions on Graphics*, 27(5), 2008.

[30] J. K. Aggarwal W. N. Martin. Volumetric descriptions of objects from multiple views. *IEEE Transactions on Pattern Analysis and Machine Intelligence*, PAMI-5(2):150–158, March 1983.

[31] Y. Le Sant, V. Todoroff, A. Bernard-Brunel, G. Le Besnerais, F. Micheli, and D. Donjat. Multi-camera calibration for 3d bos. In *Proceedings of the 17th international symposium on applications of laser techniques to fluid mechanic, Lisbon*, 2014.

[32] F. Nicolas, V. Todoroff, A. Plyer, G. Le Besnerais, D. Donjat, F. Micheli, F. Champagnat, P. Cornic, and Y. Le Sant. A direct approach for instantaneous 3d density field reconstruction from backgroundoriented schlieren (bos) measurements. *Experiments In Fluids*, 57(13), 2016.

[33] B. Hopkinson. British Ordnance Minutes, 13563, 1915.

[34] R. G. Sachs. Dependence of blast on ambient pressure and temperature. Technical Report BRL-466, Army Ballistic Research Lab, Aberdeen Proving Ground, 1944.

[35] H. Kleine, J. M. Dewey, K. Ohashi, T. Mizukaki, and K. Takayama. Studies of the TNT equivalence of silver azide charges. *Shock Waves*, 13(2):123–138, 2003.

[36] J. M. Dewey. The properties of a blast wave obtained from an analysis of the particle trajectories. *Proceedings of the Royal Society of London Series A - Mathematical and Physical Sciences*, 324(1558):275–299, 1971.

[37] J. M. Dewey. Expanding spherical shocks (blast waves). In G. Ben-Dor, O. Igra, and E. Elperin, editors, *Handbook of Shock Waves, Vol. 2*, pages 441–481. Academic Press, 2001.

[38] G. F. Kinney and K. J. Graham. *Explosive shocks in air*. Springer-Verlag, 1985.

[39] H. Hornung. Regular and mach reflections of shock waves. *Annual Review of Fluid Mechanics*, 18:33–58, 1986.

[40] Vision Research - AMETEK Material Analysis Division. *PCC 2.7 User Manual*, 2.7.756.0 edition, November 2015.

[41] L. Hunyadi. Spherefit. MATLAB Central File Exchange, 2010.

[42] P. W. Cooper. *Explosives engineering*. Wiley-VCH, Inc, 1996.

[43] D. W. Scott. On optimal and data-based histograms. *Biometrika*, 66(6):605–610, Dec. 1979.

Three-dimensional shock wave reconstruction using multiple high-speed digital cameras and background oriented schlieren imaging

by

KYLE OAKLEY WINTER